earth

MDPI

Article

Heating Rate of Light-Absorbing Aerosols from Midlatitudes to the Arctic: Implications for Arctic Warming and Northward Energy Transport

Luca Ferrero [1,*], Piotr Markuszewski [2], Martin Rigler [3], Asta Gregorič [3,4], Griša Močnik [4,5], Przemysław Makuch [2], Violetta Drozdowska [2], Małgorzata Kitowska [2], Angelo Riccio [6], Yuan-Bing Zhao [7,†], Andrea Doldi [1], Tymon Zielinski [2], Ezio Bolzacchini [1] and Niccolò Losi [1,*]

[1] GEMMA and POLARIS Centre, Università degli Studi di Milano-Bicocca, 20126 Milano, Italy; andrea.doldi@unimib.it (A.D.); ezio.bolzacchini@unimib.it (E.B.)
[2] Institute of Oceanology, Polish Academy of Sciences, 81-712 Sopot, Poland; pmarkusz@iopan.pl (P.M.); makuch@iopan.pl (P.M.); drozd@iopan.pl (V.D.); gosiak@iopan.pl (M.K.); tymon@iopan.pl (T.Z.)
[3] Aerosol d.o.o., SI-1000 Ljubljana, Slovenia; mrigler@aerosolmageesci.com (M.R.); agregoric@aerosolmageesci.com (A.G.)
[4] Center for Atmospheric Research, University of Nova Gorica, SI-5000 Nova Gorica, Slovenia; grisa.mocnik@ung.si
[5] Haze Instruments d.o.o., SI-1000 Ljubljana, Slovenia
[6] Department of Science and Application, Università degli Studi di Napoli Parthenope, 80143 Napoli, Italy; angelo.riccio@uniparthenope.it
[7] Meteorologisches Institut, Universitat Hamburg, 20148 Hamburg, Germany; yuan-bing.zhao@uni-hamburg.de or zhao1550@purdue.edu
* Correspondence: luca.ferrero@unimib.it (L.F.); niccolo.losi@unimib.it (N.L.)
† Current address: Department of Earth, Atmospheric, and Planetary Sciences, Purdue University, West Lafayette, IN 47907, USA.

Abstract

Arctic surface temperatures have increased much faster than the global mean, leading to Arctic amplification; the role of light-absorbing aerosols (LAAs; especially black carbon) in this amplification remains poorly constrained by observations. In this study, ship-borne measurements of LAAs heating rate (*HR*) from four research cruises between Europe and the Arctic were combined with reanalysis data (MERRA-2) determining a reanalysis *HR* field driving climate model simulations (CESM2). The aim was to assess how the meridional gradients in LAAs *HR* can influence Arctic warming by modulating atmospheric energy transport. LAAs *HR* declined from 335.5 ± 6.6 mK d^{-1} in summer and 254.0 ± 17.4 mK d^{-1} in winter, near Europe, to 0.9 ± 0.1 mK d^{-1} in summer, with zero *HR* inferred under polar-night conditions in winter. This gradient creates more than two orders of magnitude of atmospheric power surplus between midlatitudes and the Arctic, enhancing the poleward atmospheric meridional heat transport by 7 ± 2 and 5 ± 1 TW (summer and winter; CESM2 results). An Arctic-to-global temperature response ratio of 1.1 emerged in summer and was not meaningfully defined in winter, as the global-mean temperature response was statistically indistinguishable from zero, while the Arctic response remained positive due to the remote effect of LAAs.

Keywords: black carbon; Arctic amplification; research cruise; heating rate

Academic Editor: Charles Jones

Received: 13 September 2026
Revised: 30 October 2026
Accepted: 7 November 2026
Published: 12 November 2026

Copyright: © 2026 by the authors. Licensee MDPI, Basel, Switzerland. This article is an open access article distributed under the terms and conditions of the Creative Commons Attribution (CC BY) license.

1. Introduction

In the Arctic, near-surface temperatures are increasing four times faster than the global average [1–3], a phenomenon known as 'Arctic Amplification' (AA); this has been particularly notable since 1980, following a period of Arctic cooling, to the present time [4]. In particular, the Arctic warming has accelerated since 1980 at a rate of 0.75–1.25 °C per decade [1], reaching 3.1 °C per decade in the Eurasian Arctic in winter [5].

The causes of AA are multifaceted [6], encompassing both external drivers and internal feedback mechanisms. These include the role of greenhouse gases [4], Planck's law effect, temperature lapse rate and thermal inversion effects [7–9], and the reduction in snow and ice cover, which decreases albedo and impacts the ocean–atmosphere gas exchange and aerosol precursor emissions [7,10–12]. Additionally, changes in cloud cover, generally with positive and negative effects in winter and summer [7,8,13], and both oceanic [14,15] and atmospheric [14,16–18] heat transport significantly contribute to AA. Given their high complexity, the causes of AA have been subjected to integrated studies through: long-term monitoring at land-based stations limited by fixed positions [19–26]; measurements on mobile platforms (e.g., tethered balloons, drones, aircraft, ships, snowmobiles) operating over a wide area but being limited in time [27–35]; satellite studies partially coupling time and space [36–41]; climate model simulations covering the whole system [42,43] but being limited by the assumptions therein [44,45]. Ideally, a continuous chain from experimental measurements to modelling results is required.

Among the environmental causes affecting AA, the role of atmospheric meridional heat transport (AMHT) towards the Arctic is difficult to unravel. In fact, the magnitude and direction of the impact of AMHT on the Arctic can vary depending on the geographic location [46], seasonal timing [47,48] and analysis methodology [49]. It is noteworthy that the vast majority of studies (78%) attribute a positive contribution of AMHT to AA, while 14% report both positive and negative effects, and 8% suggest a negative impact [6]. In this context, the role of atmospheric heating due to light-absorbing aerosols (LAAs) [50–52], primarily black carbon (BC) at midlatitudes, and its influence on atmospheric meridional heat transport (AMHT) remain highly uncertain. The uncertainty arises from both the complex and often competing environmental phenomena that influence its magnitude and direction [53] and the need for a global approach that integrates spatial and temporal dimensions [45], which also requires an integrated experimental-to-modelling approach. In fact, Schmale et al. [54] distinguished the aerosol effects between local and intra-Arctic, including Arctic haze [55], new particle formation [12,56], aerosol–cloud interaction [2], vertical distribution of primary and secondary aerosols [28,29], snow darkening [57,58] and remote effects mediated by the meridional heat transport from lower latitudes [2,54].

Within the Arctic, in summer, the climatic impact of LAAs depends strongly on their vertical location [59,60]. For example, BC heats the surrounding air by absorbing solar radiation [61–64] but the resulting surface response varies with altitude: heating near the snow/ice surface may enhance warming, whereas heating in the free troposphere may induce surface cooling by increasing atmospheric stability and reducing downward sensible heat flux [59,65].

At midlatitudes, LAAs and the associated atmospheric heating are largely confined to the planetary boundary layer (PBL), close to combustion sources [64,66,67]; the resulting energy perturbation can contribute to atmospheric processes, including meridional heat transport toward the Arctic, potentially enhancing Arctic warming both in summer and winter [3,45].

This raises critical open environmental questions: (1) How large is the meridional gradient in light-absorbing aerosols (LAAs) and in their induced atmospheric heating between midlatitudes and the Arctic within the PBL? (2) To what extent does this heating

gradient, when imposed as a forcing within the PBL, affect the Arctic temperature response and the AMHT?

To answer the aforementioned questions, numerous modelling studies have explored the remote effect of aerosols on AMHT [3,4,18,20,44,45,68]. These studies were model-based, as models have been the only tools able to cover the spatial and time scales required to investigate such a phenomenon (i.e., LAAs impact on AA via AMHT). These studies suggested that a power surplus at midlatitudes, induced by the presence of LAAs (or due to reduced light-scattering aerosols), should drive AMHT towards the Arctic. Researchers [3,44,68] have found that midlatitude emission reductions since 1980 (combining all aerosol effects, sulphate and BC together) have contributed to a net Arctic surface warming, with increasing AMHT accounting for about 50% of the decadal warming trend in the Arctic, particularly in winter. Sand et al. [45] showed that atmospheric BC forcing outside the Arctic, via AMHT, may have a more substantial impact on AA than the forcing within the Arctic itself. Energy balance models have demonstrated that midlatitude BC (representing LAAs) enhanced AMHT by creating a poleward temperature gradient [14]. However, the magnitude of the remote aerosol effect on AA remains highly variable due to the uncertainties in models, such as the estimations of aerosol concentrations [44], excessively rapid ageing of aerosol and related optical properties or overly stable boundary-layer conditions in models [45]. Even when AA induced by aerosol has been modelled and unravelled (AA: 3.87 ± 0.48 compared to 2.49 ± 0.51 due to greenhouse gases) [69], both the type of aerosol responsible for such an effect and its seasonal pattern remain uninvestigated.

In fact, observational constraints on LAAs radiative effects remain critically limited, although they are required [54], particularly regarding their influence on AMHT and AA.

We addressed this gap through cross-latitudinal ship-based measurements of LAAs absorption, heating rate (*HR*), and related atmospheric power surplus (APS) from Europe to the Arctic Area, quantifying for the first time the meridional gradient in LAAs-induced atmospheric energy input, the induced AMHT and the influence on Arctic warming.

By integrating the observational data with reanalysis data (MERRA-2) and model simulations (CESM2), this research aims to provide critical new real-world observationally driven results and to refine those of previous studies, thereby offering a more accurate representation of how LAAs contribute to AA, highlighting the significance of their warming effects in both regional and global contexts; this study also opens the path for an integrated scalar approach from LAAs measurements to model results.

Therefore, the main intent of the present work was to develop a continuous logical and quantitative path from experimentally determined LAAs *HR* data to the simulated Arctic warming (within the same temporal periods as the observations). This represents a forward step in the scientific debate on Arctic amplification since, for the first time, the obtained results are derived not only from modelling activity (which remains fully valuable) but also from a hybrid approach based on both experimental and reanalysis data. By doing so, the present work directly determines the atmospheric LAAs *HR*, reducing the dependence on model assumptions related to LAAs emissions, optical properties and mixing state [44,45,70].

2. Materials and Methods

The methodological approach followed a logical path based on three pillars required to answer the scientific questions reported in the Section 1; the three pillars were:

1. The ship-borne experimental measurements of LAAs *HR* from midlatitudes to the Arctic, providing a unique starting database;
2. The spatialization of the LAAs HR into a reanalysis *HR* field constrained by ship-borne observations using reanalysis data (MERRA-2);

3. The modelling simulations of atmospheric warming and related AMHT via CESM2, using the *HR* field as input constrained by shipborne observations.

2.1. Measurement Campaign

LAAs concentration and *HR* were experimentally determined from midlatitudes to the Arctic through ship-borne measurements carried out aboard the R/V Oceania, operated by the Institute of Oceanology, Polish Academy of Sciences (Figure S1). The feasibility of such measurements had been tested in previous campaigns [27,71], and the R/V Oceania had operated in the last two decades following the same basic route from Europe to the Arctic.

With respect to the present study, three summer ARctic EXpeditions campaigns (AREX 2018, 2019 and 2021; 54–80° N) were carried out from mid-June to mid-September, starting in Gdansk and moving along the Baltic, North Atlantic and the Arctic Ocean (Figure S2a–c). Additionally, a winter BALTIC campaign (2022) was carried out from 54° N to 63° N (Figure S2d) over the Baltic Sea. It is evident that while AREX campaigns measured LAAs *HR* as far as the Arctic, the BALTIC campaign did not reach it, limiting the track to 63° N. As the R/V Oceania is not an icebreaker, the purpose of the last BALTIC campaigns was to measure the LAAs *HR* gradient from midlatitudes to the closest area to the darkness of the Arctic night until sea ice prevented further northward navigation; in this respect, reaching 63° N enabled the determination of the value of LAAs *HR* immediately before its drop to zero in the absence of sunlight in the winter polar night. Going deeper, the BALTIC campaign aimed at finding a suitable calibration factor (see Section 2.3.2) for wintertime MERRA-2 data up to a latitude above which the contribution of solar radiation sharply decreased, leading to the absence of LAAs *HR*; in fact, in order to determine the midlatitude-to-Arctic warming impact of LAAs, it is not necessary to know the LAAs concentrations within the Arctic itself, where sunlight is absent and shortwave LAAs *HR* is therefore zero. We acknowledge that the BALTIC campaign cannot be used to determine the LAAs mass concentrations in the Arctic, which is beyond the possibilities afforded by data availability.

The ship-borne approach also enabled us to address the challenge of the sparsity and lack of representativeness of individual monitoring stations in the Arctic, given the vastness of this region [27,54].

The instrumentation and details of Oceania's cruises are comprehensively described in Losi et al. [71] and Ferrero et al. [27,72]. Here, a brief summary is provided. Multiwavelength LAAs measurements were performed using the aethalometer AE33 (Aerosol Magee Scientific d.o.o., Slovenia). BC concentrations were reported as MeBC (median equivalent BC) following the protocol of Savadkoohi et al. [73] to ensure comparability with other European and worldwide monitoring sites. The MeBC data were reported at ambient temperature and pressure, and the raw data were processed by removing spikes due to vessel exhaust interference by applying a vessel speed/apparent wind filter (180 ± 40°) before averaging, as detailed in Losi et al. [71]; due to Oceania's tendency to sail headwind and the greater height of the chimney above the sampling line, only a small percentage of data (less than 2%) were affected by the ship's emissions and were discarded [71]. As a second step, MeBC data were treated with a 30 min mean step, corresponding to a maximum latitudinal spatial resolution of 9 km, given the average speed of the Oceania ship.

Broadband and hyperspectral direct, diffuse and reflected radiation were also measured onboard the R/V Oceania; this was done using one pyranometer and a spectroradiometer installed on Oceania's balcony.

The broadband shortwave radiation was measured by an SPN1 pyranometer coupled with a GP1 Data Logger (Delta-T Devices, Cambridge, UK) providing 3 outputs:

global solar radiation, diffuse radiation and sunshine status. Its hexagonal arrangement of seven radiation sensors and a patented hemispherical shadow mask allows diffuse radiation measurements without moving parts, regardless of the sun's position. Direct solar radiation was obtained by subtracting the diffuse component from the total; in this respect, the tilt of the SPN1 due to the ship's motion was corrected using a well-established method [74,75], based on the sun's position (solar zenith and azimuth angles) and the angle of incidence on the tilted instrument plane calculated from the ship's orientation values (pitch, roll and yaw from an Ellipse-E Inertial Navigation Sensor, by SBG Systems). SPN1 data enabled cloudiness determination (expressed in oktas) following Ehnberg and Bollen [76] as demonstrated in previous work [77].

The hyperspectral radiation measurements were performed using a RoX spectroradiometer (JB Hyperspectral Devices, Düsseldorf, Germany) installed on Oceania's measurement platform. It is based on the Multiplexer Radiometer Irradiometer (MRI) described in the work of Cogliati et al. [78] and used in previous works to experimentally determine the LAAs *HR* [77,79,80]; the RoX spectroradiometer collects incident and reflected radiation in the visible/near infrared region (300–1000 nm) by exploiting the Flame spectrometer from Ocean Optics (Orlando, FL, USA). The RoX used during the campaigns was equipped with a gimbal and a rotating shadowband. The gimbal compensated for ship motion, eliminating the need for the post-data correction required by the SPN1. The shadowband rotated at 5 degrees per minute, covering the whole of the upwelling sensor's field of view. Consequently, global irradiance was measured when the sensor was uncovered, while diffuse irradiance was measured when the band shaded it. This setup allowed for the separation of diffuse radiation from the global component and also the determination of direct radiation by subtracting the direct component from the total [79]. AE33, SPN1 and RoX acquired data at the same time resolution of 1 min.

2.2. LAAs Heating Rate

The LAAs heating rate was obtained by combining the LAAs multi-wavelength absorption coefficient $b_{abs}(\lambda)$ and multi-wavelength radiation measurements (direct, diffuse or reflected), over the entire 2π hemisphere, from both the sky and the surface, under the isotropic and Lambertian assumptions, as follows [67,69–71]:

$$HR = \frac{1}{\rho C_p} \cdot ADRE = \frac{1}{\rho C_p} \cdot \left[\frac{1}{cos(\theta_z)} \int_{\lambda} F_{dir}(\lambda)\, b_{abs}(\lambda)\, d\lambda + 2 \int_{\lambda} F_{dif}(\lambda)\, b_{abs}(\lambda)\, d\lambda + 2 \int_{\lambda} F_{ref}(\lambda)\, b_{abs}(\lambda)\, d\lambda \right] \quad (1)$$

where

ADRE is the absorptive direct radiative effect (W m^{-3}), representing the power of solar energy absorbed by the LAAs and converted into heat per unit volume in the atmosphere;
θ_z refers to the solar zenith angle,
$F_{dir}(\lambda)$, $F_{dif}(\lambda)$ and $F_{ref}(\lambda)$ are the spectral direct, diffuse and reflected irradiances;
ϱ represents the air density (kg m^{-3});
C_p (1005 J kg^{-1} K^{-1}) is the isobaric specific heat of dry air.

For the aethalometer data, Equation (1) can be rewritten as follows [80,81]:

$$HR = \frac{1}{\rho C_p} \cdot \frac{1}{C} \cdot \left[\frac{1}{cos(\theta_z)} \int_{\lambda} F_{dir}(\lambda)\, b_{ATN_LC}(\lambda)\, d\lambda + 2 \int_{\lambda} F_{dif}(\lambda)\, b_{ATN_LC}(\lambda)\, d\lambda + 2 \int_{\lambda} F_{ref}(\lambda)\, b_{ATN_LC}(\lambda)\, d\lambda \right] \quad (2)$$

where

$b_{ATN_LC}(\lambda)$ is the wavelength-dependent attenuation coefficient corrected for the loading (an automatic process in the aethalometer AE33 [82]);
C is the multiple-scattering correction parameter that compensates for the multiple scattering of light induced by the filter fibres and by the particles embedded in the filter.

Equation (2) shows that, once the *ADRE* and *HR* have been determined with a specific *C* value, it is always possible to rescale the data using a different *C* value, allowing future data adjustment: in fact, aethalometers also have the advantage of global long-term data series [83] that could be used in the near future to retrieve historical series of the *HR*. For the purpose of the present work, a reliable determination of $b_{abs}(\lambda)$, and then of *C*, is required. Up to now, neither a commonly accepted unique reference instrument [52,84,85] nor a reference material [86] exists for the measurement of the aerosol absorption coefficient; commonly used standard reference devices (e.g., CAPS, MAAP, PAX, PTAAM) are not available together with aethalometers at each measuring site around the world or on small ships such as the R/V Oceania. Therefore, Backman et al. [87] and the ACTRIS community [73,88] suggested using a common *C* of 2.45 for the AE33 equipped with M8060 filter tape (obtained as the product of the manufacturer *C* of 1.39 and the ACTRIS harmonization factor of 1.76). This enables the comparability of results obtained at different sites. However, the real *C* values can vary greatly, e.g., in the 2.23–4.24 range [89] and above [90] in different seasons and locations. Thus, the *C* parameter was determined through a novel methodology that provides a MAAP-like C_{AE} from the aethalometer loading parameters k as follows:

$$C_{AE} = C_{ref} + \alpha_{AE} \frac{SSA_{AE}}{(1 - SSA_{AE})} = C_{ref} + \alpha_{AE} \frac{m \cdot (1 - 50 \cdot k) - 50 \cdot k}{50 \cdot k} \quad (3)$$

where C_{AE} refers to the *C* obtained at 660 nm wavelength directly from the AE33 loading *k* data; it is noteworthy that the aforementioned methodology can be used starting from the AE33 loading *k* data at the other wavelengths, as the methodology is calibrated to always result in an equivalent wavelength of C_{AE} at 660 nm. Details and validation are beyond the aim of the present work, as fully reported by Ferrero et al. [90], to whom we refer. C_{ref} and α_{AE} are the reference multiple-scattering filter parameter (which depends only on the filter properties) and the scattering fraction parameter, respectively; they equal 1.810 (±0.028) and 0.2154 (±0.009) using the *k* values at 470 nm as input. In fact, the 470 nm channel presented 0% of negative *k* values along the whole AREX path [90]. Finally, SSA_{AE} refers to the single-scattering albedo of the aerosol estimated on the aethalometer's surface filter tape (at 470 nm in this case), *m* (0.86 ± 0.06) is the Weingartner et al. [91] empirical parameter, and *k* is the averaged value of the aethalometer loading parameters for each latitudinal degree.

Thus, the $b_{abs}(\lambda)$ values were retrieved as follows:

$$b_{abs(\lambda)} = \frac{b_{ATN_LC(\lambda)}}{C_{AE}} \quad (4)$$

The method described using Equations (3) and (4) has been validated in Ferrero et al. [90] and has already been used in the Arctic, leading to reliable results; we refer to the aforementioned work for further details.

Tables S1 and S2 report the latitudinal C_{AE} values together with those of SSA_{AE} and MeBC. The C_{AE} values are in line with the harmonized *C* factor of 2.45 suggested by ACTRIS [88] (https://www.actris-ecac.eu/ accessed on 30 October 2026) close to Europe; moving towards the Arctic, C_{AE} increased [87] in line with SSA_{AE} [90]. Therefore, using the appropriate latitudinal C_{AE} values helped avoid errors in *ADRE* and *HR* that could have exceeded 100% if a fixed *C* had been used instead [87,89,90,92]. This is particularly important for this work, as it is based on the LAAs *HR* latitudinal gradients.

Once the $b_{abs}(\lambda)$ values are determined, they can be (1) apportioned for carbonaceous species (i.e., black and brown carbon, BC and BrC) and (2) used as a whole or in the apportioned form to determine the atmospheric HR due to the absorbing aerosols released into the atmosphere. Assuming that BrC $b_{abs}(\lambda)$ is negligible in the infrared and that the absorption angstrom exponent of BC is equal to 1, enables the decoupling of the contribution of the two most important LAAs species, as reported in previous studies, to which

we refer for further details [81,93]. We underline that an environmental discussion concerning sources and related species of LAAs from midlatitudes to the Arctic is beyond the present work, as a dedicated campaign for this purpose was already carried out in 2024 within the project GAIA (New Integrated Experimental and Modelling Tools for Georeferenced Source Apportionment of Aerosol Climate-Relevant Parameters from the Mediterranean Area up to the Arctic). Here, the BC-BrC splitting has the sole purpose of discussing the reliability of using MERRA-2 data to spatialize the assessment of LAAs *ADRE* and *HR* (Section 2.3).

2.3. A New Method for Determining LAAs HR from Reanalysis Data

MERRA-2 (Modern-Era Retrospective analysis for Research and Applications, version 2) data were used to determine the *ADRE* and the *HR* of LAAs across a range of latitudes and longitudes to encompass the cruise track and provide the observationally driven data for modelling simulations (Section 2.4).

Surface BC concentration, surface shortwave incoming global solar irradiance (I_{glo}), surface albedo and planetary boundary layer (PBL) height, temperature and pressure data were collected and used. They are products obtained from the Giovanni online data system, developed and maintained by NASA GES DISC. All data are available on the same horizontal grid with a resolution of 0.625° × 0.5° longitude-by-latitude. Monthly averages were determined from hourly data in all-sky conditions, considering the 3 months and the 3 years (2018, 2019 and 2021) that covered the summer AREX campaigns, and February 2022 for the winter campaign. These data enabled us to get the output of pillar 2 of the present methodology: the large-scale spatial structure of the *HR* used for driving modelling simulations. In fact, the monthly MERRA-2 averages were the necessary conditions to match the ship cruise period, enabling the determination of whether the ship-borne observation of the LAAs *HR* gradient persisted while the ship moved.

To achieve this goal, the ADRE and *HR* computations were performed on reanalysis data from midlatitudes (40° N) to the Arctic, starting from the surface BC concentration, shortwave incoming radiation and surface albedo; this approach enabled us to highlight the potential amount of energy trapped in the atmosphere by LAAs, potentially available for the AMHT and related Arctic warming.

A full demonstration of the developed methodology is reported below. We briefly summarize it here to guide the reader. First, it is noteworthy that MERRA-2 data contain the basic variables needed: BC concentration as the most abundant LAAs species worldwide, radiation from the sun and sky (global irradiance) and from the surface (computed from irradiance and albedo). Despite this, the MERRA-2 fields used here lack the absorption coefficient and the spectral irradiance required by Equation (1) for *HR* determination. Therefore, the following derivation addresses these limitations formally. The absence of the absorption coefficient is resolved by exploiting the linear relationship between BC mass concentration and the absorption coefficient via a proper mass absorption cross section (MAC). The lack of spectral irradiance data is addressed formally through the weighted integral representation of Equation (1). As a result, it is observed that a component-specific effective MAC enters the broadband representation after spectral integration. This means that, among all the possible values of MAC at different wavelengths, an effective MAC is defined for each radiative component, as it combines in one value both the mass-to-absorption properties and the spectral dependence of absorption and incident radiation. The final solution is the one shown in Equation (12) and then in Equation (14). Further, the effective MAC is calibrated by using the experimental data collected along the ship-borne campaigns. The full demonstration of the developed methodology for using reanalysis data to determine the *ADRE* and *HR* is detailed below.

2.3.1. Formal Demonstration of the Methodology

From Equation (1), the *ADRE* can be determined as follows:

$$ADRE = \frac{1}{cos(\theta_z)} \int_{\lambda} F_{dir}(\lambda)\, b_{abs}(\lambda)\, d\lambda + 2 \int_{\lambda} F_{dif}(\lambda)\, b_{abs}(\lambda)\, d\lambda + 2 \int_{\lambda} F_{ref}(\lambda)\, b_{abs}(\lambda)\, d\lambda \quad (5)$$

where each term of the summation represents an integral over the entire shortwave solar spectrum of the product $F_n(\lambda)\, b_{abs}(\lambda)$, where n stands for the n^{th} kind of spectral resolved impinging irradiance: direct, diffuse and reflected.

Equation (5) shows that, to derive the *ADRE* on a wide spatial domain from reanalysis data, $b_{abs}(\lambda)$ and $F_n(\lambda)$ must be known.

However, the MERRA-2 fields used here provide BC mass concentrations (the most important LAA species; Figure S3 in Supplementary Materials), surface shortwave incoming global solar irradiance (I_{glo}) and surface albedo.

Therefore, first, Equation (5) was rewritten to be used depending on the aforementioned parameters and later used for environmental applications; this reformulation begins solving the generic integral $\int_{\lambda_{min}}^{\lambda_{max}} F_n(\lambda)\, b_{abs}(\lambda)\, d\lambda$ in Equation (5) (λ_{min} and λ_{max} are the extremes of the shortwave spectrum), which can be rewritten in parts as follows:

$$\int_{\lambda_{min}}^{\lambda_{max}} F_n(\lambda)\, b_{abs}(\lambda)\, d\lambda = I_n(\lambda_{max})\, b_{abs}(\lambda_{max}) - I_n(\lambda_{min})\, b_{abs}(\lambda_{min}) - \int_{\lambda_{min}}^{\lambda_{max}} I_n(\lambda) b'_{abs}(\lambda)\, d\lambda \quad (6)$$

where $b'_{abs}(\lambda) = \frac{\mathrm{d}}{\mathrm{d}\lambda} b_{abs}(\lambda)$, while the broadband irradiance terms $I_n(\lambda_{max})$ and $I_n(\lambda_{min})$ represent integrals of the spectrally resolved incident irradiance ($F_n(\lambda)$) evaluated at the limits of the shortwave spectrum, λ_{min} and λ_{max}, respectively. It is noteworthy that $I_n(\lambda)$ is the cumulative function of the solar spectrum, with $I_n(\lambda_{min}) = 0$ at λ_{min} and $I_n(\lambda_{max}) = I_{n_tot}$ representing the total broadband irradiance. This can be formalized by the following Equation (7):

$$I_{n_tot} = I_n(\lambda_{max}) - I_n(\lambda_{min}) = \int_{\lambda_{min}}^{\lambda_{max}} F_n(\lambda)\, d\lambda \quad (7)$$

Consequently, the term $I_n(\lambda_{min})\, b_{abs}(\lambda_{min}) = 0$ in Equation (6), and the same equation becomes:

$$\int_{\lambda_{min}}^{\lambda_{max}} F_n(\lambda)\, b_{abs}(\lambda)\, d\lambda = I_{n_tot}\, b_{abs}(\lambda_{max}) - \int_{\lambda_{min}}^{\lambda_{max}} I_n(\lambda) b'_{abs}(\lambda)\, d\lambda = I_{n_tot} \cdot BC \cdot MAC(\lambda_{max}) - \int_{\lambda_{min}}^{\lambda_{max}} I_n(\lambda) \cdot b'_{abs}(\lambda)\, d\lambda \quad (8)$$

where $b'_{abs}(\lambda) = \frac{\mathrm{d}}{\mathrm{d}\lambda} b_{abs}(\lambda) = \frac{\mathrm{d}}{\mathrm{d}\lambda} BC \cdot MAC(\lambda) = BC \cdot \frac{\mathrm{d}}{\mathrm{d}\lambda} MAC(\lambda)$ in the case of an *ADRE* and an *HR* BC dominated (among all possible LAAs species), where MAC is the BC mass absorption cross-section; in this respect, Figure S3 (Supplementary Materials) shows that BC was the main component of *ADRE* and *HR* experimentally determined during the cruises: *HR* due to BC was more than 90% of the total, in keeping with previous values obtained in Europe [77]. Thus, the right side of Equation (8) can be written as:

$$I_{n_tot} \cdot BC \cdot MAC(\lambda_{max}) - \int_{\lambda_{min}}^{\lambda_{max}} I_n(\lambda) \cdot BC \cdot \frac{\mathrm{d}}{\mathrm{d}\lambda} MAC(\lambda)\, d\lambda = I_{n_tot} \cdot BC \cdot MAC(\lambda_{max}) - BC \cdot \int_{\lambda_{min}}^{\lambda_{max}} I_n(\lambda) \cdot \frac{\mathrm{d}}{\mathrm{d}\lambda} MAC(\lambda)\, d\lambda \quad (9)$$

To solve Equation (9), it is necessary to handle the right-side integral $\int_{\lambda_{min}}^{\lambda_{max}} I_n(\lambda) \cdot \frac{\mathrm{d}}{\mathrm{d}\lambda} MAC(\lambda)\, d\lambda$; within this term, both $I_n(\lambda)$ and $MAC(\lambda)$ vary with the wavelength, thus requiring careful treatment to avoid any approximation error. In the following equation (Equation (10)), the aforementioned integral is solved using integration by parts together with the "mean value theorem for weighted integrals" as follows:

$$\begin{gathered} \int_{\lambda_{min}}^{\lambda_{max}} I_n(\lambda) \cdot \frac{\mathrm{d}}{\mathrm{d}\lambda} MAC(\lambda)\, d\lambda = I_n(\lambda_{max}) \cdot MAC(\lambda_{max}) - I_n(\lambda_{min}) \cdot MAC(\lambda_{min}) - \int_{\lambda_{min}}^{\lambda_{max}} F_n(\lambda) \cdot MAC(\lambda)\, d\lambda = I_n(\lambda_{max}) \cdot MAC(\lambda_{max}) - I_n(\lambda_{min}) \cdot MAC(\lambda_{min}) - MAC(\lambda_{\xi}) \cdot \int_{\lambda_{min}}^{\lambda_{max}} F_n(\lambda)\, d\lambda = I_{n_tot} \cdot MAC(\lambda_{max}) - MAC(\lambda_{\xi}) \cdot I_{n_tot} \end{gathered} \quad (10)$$

Let us explain the results obtained in Equation (10). As noted above, $I_n(\lambda_{max}) = I_{n_tot}$, while $I_n(\lambda_{min}) = 0$, so the second term in the sum vanishes. $MAC(\lambda_\xi)$ represents instead the output of the application of the "mean value theorem for weighted integrals": over the integration interval (λ_{min}–λ_{max}), if $F_n(\lambda)$ is non-negative and integrable, and $MAC(\lambda)$ is continuous, then there exists an effective wavelength ξ between λ_{min} and λ_{max} such that $\int_{\lambda_{min}}^{\lambda_{max}} F_n(\lambda) \cdot MAC(\lambda)\, d\lambda = MAC(\lambda_\xi) \cdot I_{n_tot}$.

In this respect, $MAC(\lambda_\xi)$ combines in one value both the mass-to-absorption properties of LAAs and spectral weighting by radiation; $MAC(\lambda_\xi)$, at an effective wavelength ξ is a radiation-weighted effective quantity for the specified radiative component. This means that, among the whole possible values of MAC at different wavelengths, the MAC at a wavelength ξ depends on the incident spectrum, as it combines the spectral dependence of aerosol absorption and incident radiation.

Using this concept, and substituting Equation (10) into Equations (8) and (9), it follows that:

$$\int_{\lambda_{min}}^{\lambda_{max}} F_n(\lambda)\, b_{abs}(\lambda)\, d\lambda = I_{n_tot} \cdot BC \cdot MAC(\lambda_{max}) - I_{n_tot} \cdot BC \cdot MAC(\lambda_{max}) + I_{n_tot} \cdot BC \cdot MAC(\lambda_\xi) = I_{n_tot} \cdot BC \cdot MAC(\lambda_\xi) \quad (11)$$

Finally, Equation (11) is inserted in Equation (5) for each radiation component, as follows:

$$ADRE = BC \cdot \left[MAC_{dir}(\lambda_{\xi_dir}) \cdot \frac{1}{\cos(\theta_z)} I_{dir} + MAC_{dif}(\lambda_{\xi_dif}) \cdot 2I_{dif} + MAC_{ref}(\lambda_{\xi_ref}) \cdot 2I_{ref} \right] \quad (12)$$

The *ADRE* in Equation (12) can be easily converted to *HR* using Equation (1) and the air density derived from temperature and pressure.

The present equation (Equation (12)) represents an important result of the present work, as it allows us to compute the *ADRE* (and therefore the *HR*) starting from the mass concentration of BC once the component-specific effective $MAC(\lambda_\xi)$ values are known for direct, diffuse and reflected broadband irradiances.

$MAC_n(\lambda_{\xi_n})$ values (n stands for the nth kind of radiation) can be determined considering that each term of the sum on the right side of Equation (12) represents the direct, diffuse and reflected component of *ADRE*: $ADRE_{dir}$, $ADRE_{dif}$ and $ADRE_{ref}$, respectively [79]; therefore, at a site with non-zero BC and component irradiance, it is possible to determine $MAC_n(\lambda_{\xi_n})$ values by inverting each term of Equation (12):

$$MAC_{dir}(\lambda_{\xi_dir}) = \frac{ADRE_{dir}}{BC \cdot \left[\frac{1}{\cos(\theta_z)} I_{dir}\right]};\ MAC_{dif}(\lambda_{\xi_dif}) = \frac{ADRE_{dif}}{BC \cdot [2I_{dif}]};\ MAC_{ref}(\lambda_{\xi_ref}) = \frac{ADRE_{ref}}{BC \cdot [2I_{ref}]}; \quad (13)$$

The approach described in Equation (12) can be used in either of these situations:

1. In most of the world measurement stations where the aforementioned parameters can be available;
2. On a large scale by using reanalysis data that provide BC and the required radiation data.

In order to apply Equation (12) using the MERRA-2 products, it must be noted that the MERRA-2 fields used here provide BC, I_{glo} and the surface albedo, while I_{dir} and I_{dif} are not included in these fields. They (I_{dir} and I_{dif}) should be available from the Copernicus radiation data (https://ads.atmosphere.copernicus.eu/datasets/cams-gridded-solar-radiation?tab=overview; accessed on 30 October 2026), despite the limitation that this gridded product does not cover the full Arctic and open-ocean domain. To cover the Arctic area using the same data source from midlatitudes, the MERRA-2 data were used. Therefore,

the application of Equation (12) to the MERRA-2 database and the determination of the corresponding MAC values are discussed in the next Section 2.3.2.

Once the *ADRE* is determined, it can be integrated over time or over height (up to the planetary boundary layer top) to obtain the so-called atmospheric power surplus (*APS*, J d^{-1} m^{-3}) or the total atmospheric APS_{COL} (W m^{-2}), whose purpose is to estimate the energy released as heat in the atmosphere by LAAs (in a given period of time) to highlight the amount of energy available to all those atmospheric processes related to its conservation such as atmospheric energy storage, radiative adjustment, surface exchange and horizontal energy divergence.

2.3.2. Application to MERRA-2 Products and Environmental MAC Determination

Equation (12) is of general application and gives the possibility to compute the *ADRE* (and therefore the *HR*) starting from the mass concentration of BC once $MAC_n(\lambda_{\xi_n})$ is well defined for direct, diffuse and reflected broadband irradiances. However, the weighted mean value theorem applies to each radiative component separately, provided its spectral weighting function is non-negative and integrable and MAC is continuous over the wavelength interval. The corresponding effective wavelength ξ may therefore differ among the direct, diffuse and reflected components, and equal component MAC values are not guaranteed by the theorem: combined effective MAC requires irradiance and angular weighting.

However, as aforementioned, the MERRA-2 fields used here provide BC, I_{glo} and the surface albedo, while I_{dir} and I_{dif} are not available.

Therefore, to use MERRA-2 data, Equation (12) was reformulated; let us define X as the global irradiance fraction due to the direct component defined as $X = I_{dir}/I_{glo}$. Equation (12) was then approximated empirically as follows:

$$\begin{aligned} ADRE &= BC \cdot \left[MAC_{dir}\left(\lambda_{\xi_{dir}}\right) \cdot \frac{1}{\cos(\theta_z)} I_{dir} + MAC_{dif}\left(\lambda_{\xi_{dif}}\right) \cdot 2I_{dif} + MAC_{ref}\left(\lambda_{\xi_{ref}}\right) \cdot 2I_{ref} \right] \\ &= BC \\ &\cdot \left[2I_{glo} \cdot \left(\frac{MAC_{dir}\left(\lambda_{\xi_{dir}}\right) X + 2\, MAC_{dif}\left(\lambda_{\xi_{dif}}\right)(1 - \mathrm{X})\cos(\theta_z) + 2\, MAC_{ref}\left(\lambda_{\xi_{ref}}\right) Albedo \cos(\theta_z)}{2\cos(\theta_z)} \right) \right] \\ &\approx BC \cdot \left[2I_{glo} \cdot \left(\frac{2\, MAC_{dif}\left(\lambda_{\xi_{dif}}\right)\cos(\theta_z) + 2\, MAC_{ref}\left(\lambda_{\xi_{ref}}\right) Albedo \cos(\theta_z)}{2\cos(\theta_z)} \right) \right] \\ &\approx BC \cdot eMAC \cdot \left[2I_{glo} \cdot (1 + Albedo) \right] \end{aligned} \quad (14)$$

where *eMAC* describes an empirical environmental MAC that is obtained when $[2I_{glo}(1+Albedo)]$ is used as a broadband proxy for the radiation terms on the right-hand side of Equation (12).

The approximated solution of Equation (12) can be obtained under two conditions: (1) when $MAC_{dir}(\lambda_{\xi_dir})X$ can be neglected relative to the other terms due to the dominant role of diffuse radiation and the lower value of $MAC_{dir}(\lambda_{\xi_dir})$ compared to $2MAC_{dif}(\lambda_{\xi_dif})$ and $2MAC_{ref}(\lambda_{\xi_ref})$, provided X is also small; (2) when $MAC_{dif}(\lambda_{\xi_dif}) \approx MAC_{ref}(\lambda_{\xi_ref})$. This empirical approximation is assessed below.

In the present work, the diffuse component of global irradiance was dominant during the campaign (as reported in the following Section 3 of the Results including Figures 2 and 3). In particular, the summertime diffuse radiation fraction (68.4 ± 5.0% of I_{glo} and up to 75.6 ± 6.0% of I_{glo} above 70° N) dominated under the cloudy conditions of the campaigns (5.4 ± 0.3 oktas, up to 6.2 ± 0.4 oktas above 70° N, Figure S4); during winter, even in the Baltic, the cloud coverage (4.86 ± 0.32 oktas) dominated (Figure S5). This is in keeping with previously reported cloud cover values in Losi et al. [71]. $MAC_{dir}(\lambda_{\xi_dir})$, $MAC_{dif}(\lambda_{\xi_dif})$ and $MAC_{ref}(\lambda_{\xi_ref})$ were determined during the cruises by fitting Equation (13) using the experimental $ADRE_{dir}$, $ADRE_{dif}$, $ADRE_{ref}$ radiation and MeBC data; they were, respectively, 7.0 ± 0.2, 9.0 ± 0.2 and 8.6 ± 0.1 m^2 g^{-1} in summer and 7.0 ± 0.5, 12.4 ± 0.9 and 10.1 ± 1.1 m^2 g^{-1} in

winter. Therefore, $MAC_{dir}(\lambda_{\varepsilon_dir})$ is less than half of $2MAC_{dif}(\lambda_{\varepsilon_dif})$ and $2MAC_{ref}(\lambda_{\varepsilon_ref})$ in both summer and winter. Finally, the above data permitted the assessment of the $MAC_{dif}(\lambda_{\varepsilon_dif}) \approx MAC_{ref}(\lambda_{\varepsilon_ref})$ assumption, with a small discrepancy in winter.

Therefore, from Equation (14), the empirical environmental mass absorption cross section (*eMAC*) was computed by inverting the equation as follows, using the experimental total *ADRE*, MeBC and radiation data obtained from ship cruises:

$$eMAC \approx \frac{ADRE}{MeBC \cdot \left[2I_{glo} \cdot (1 + Albedo)\right]} \quad (15)$$

The *eMAC* data were obtained through an internal cross-validation procedure detailed hereinafter. Before using *eMAC* with MERRA-2 data (Section 3.2), the *eMAC* values were determined and tested. A leave more-out (LMO), three-fold interleaved cross-validation procedure was used, dividing the dataset into three parts (two for training and one for evaluation) to assess the model's predictive performance using three training/evaluation splits per season. The cross-validation approach consisted of splitting the whole dataset into two parts, the first one used to train the model and the second one used to evaluate its predictive performance. The criterion used in splitting the data was an interleaved evaluation set spanning the latitude range due to the higher latitudinal gradients of the variables (*ADRE* and radiation) involved in the analysis; therefore, one observation out of every 3 was selected, from the original dataset, to generate the evaluation set. In this way, the same proportion of low-latitude and high-latitude data was maintained both in the training and in the evaluation set. By choosing the training and evaluation sets differently three times (with the aforementioned criteria), it was possible to train three calibration models, assessing the model's predictive performance, and obtain 3 possible tests per season. This allowed the seasonal *eMAC* parameter to be obtained as the average of the three models. This approach has previously been successfully applied in other validation studies to which we refer [90,94].

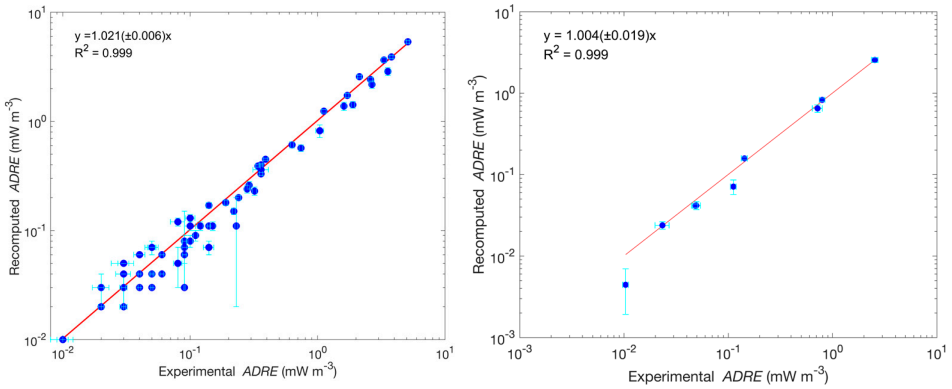
This computation resulted in an average *eMAC* value of 8.7 ± 0.1 $m^2\ g^{-1}$ in summer and 12.7 ± 0.3 $m^2\ g^{-1}$ in winter; the obtained *eMAC* empirically embeds both the approximation introduced in Equation (14) and the small fraction of *ADRE* due to species other than BC. The uncertainty of *eMAC* (± 0.1 and ± 0.3 $m^2\ g^{-1}$, in summer and winter) represented 1.1 and 2.4% of the *eMAC* values. This is the calibration component of the relative uncertainty propagated onto the MERRA-2 *HR* estimates, excluding input-data and calibration-transfer uncertainties.

The validation results are reported in Figure 1 (the predicted *ADRE* vs. the measured *ADRE*). The high R^2 (0.999) during both summer and winter, the slopes close to ~1 and the low absolute mean relative error (~4%) indicated the internal consistency of the developed methodology in reproducing the measurement-derived *ADRE* and *HR* within these campaigns using BC mass concentrations and broadband shortwave radiation data, which are available in MERRA-2 products. This enabled the provision of an energy map from Europe to the Arctic for the subsequent modelling simulations (Section 2.4).

From an environmental point of view, the *eMAC* values are consistent with recent findings across Europe for aethalometers [73,88], which reported values of 7.8 ± 3.4 $m^2\ g^{-1}$. Moreover, to check the *eMAC* reliability in different areas, previously published ADRE and HR data [77,81] were used to retrieve *eMAC* (using Equation (15) on a seasonal basis: in Milan [77] the *eMAC* was 9.0 ± 0.1 (spring), 9.6 ± 0.1 (summer), 9.8 ± 0.1 (autumn) and 13.4 ± 0.2 (winter) $m^2\ g^{-1}$ while, in Schivenoglia (Po Valley) [81] it was 12.4 ± 0.2 $m^2\ g^{-1}$ in late autumn showing a growing tendency from summer to winter as found from AREX to BALTIC campaigns.

Finally, to check the sensitivity of the obtained *eMAC* to the radiation weighting, effective MAC values were also determined from Equation (12) checking the possibility of using a radiation-weighted effective MAC (that also accounts for direct radiation) by

defining a weighted average and extracting it from the right side of Equation (12) leaving $BC \cdot eMAC \left[\frac{1}{\cos(\theta_z)} I_{dir} + 2I_{dif} + 2I_{ref}\right]$. Results were 8.3 ± 0.1 m² g⁻¹ in summer and 11.8 ± 0.5 m² g⁻¹ in winter (uncertainties 1.2% and 4.2%, respectively) with values approximately 5% and 7% lower than empirical *eMAC* estimated without direct component. This is due to the fact that the broadband proxy $\left[2I_{glo} \cdot (1 + Albedo)\right]$ in Equation (14) represents 90 ± 1% of the full angularly weighted irradiance $\left[\frac{1}{\cos(\theta_z)} I_{dir} + 2I_{dif} + 2I_{ref}\right]$ leading (with the same *ADRE* and MeBC) to higher empirical *eMAC* estimates.



(**a**) (**b**)

Figure 1. Linear correlation between the experimental and recomputed *ADRE* during the AREX (**a**) and BALTIC (**b**) cruises.

Hereinafter, the *eMAC* values of 8.7 ± 0.1 m² g⁻¹ in summer and 12.7 ± 0.3 m² g⁻¹ in winter will be used together with the black carbon concentration and the global radiation and albedo data from MERRA-2. In this respect, we acknowledge that the internal cross-validation shown in Figure 1 does not constitute a validation of the MERRA-2 input data. MERRA-2 input data have their own uncertainties, the validation of which is beyond the purpose of the present work. Moreover, as a final remark, the exact integral representation (Equation (12)) and the empirical broadband approximation used with MERRA-2 (Equation (14)) should be kept distinct, as the latter requires independent validation when transferred to other environmental conditions.

2.4. CESM2 Modelling Simulations

To complement the findings from observational analyses, modelling simulations were conducted using the Community Earth System Model version 2.2 (CESM2) [95]; the simulations were based on the reanalysis *HR* field obtained from MERRA-2 data constrained by shipborne observations (Section 2.3). CESM2 simulations were performed on the DKRZ Levante supercomputer (the high-performance computing system at the German Climate Computing Center, DKRZ) using the full year's available computing resources devoted to the present work.

CESM2 was configured in atmosphere-only mode, which includes interactive atmosphere and land-surface components with prescribed climatological monthly varying sea surface temperatures (SSTs) and sea ice concentrations [96]. The atmospheric component, Community Atmosphere Model version 6 (CAM6) [97], and the land-surface component, Community Land Model version 5 (CLM5) [98], were used with a horizontal resolution of 0.9° latitude by 1.25° longitude. CAM6 employs a hybrid sigma-pressure vertical coordinate with 32 levels.

The modelling design was based on the single-model initial-condition large-ensemble approach (SMILE) [99], comprising 140 paired control and perturbed simulations

corresponding to the same time periods as the experimental ship-based LAAs measurements; the ensemble pairs were obtained without/with (control/perturbed) the spatial data of the LAAs *HR* with restart files saved annually on January 1st. Therefore, the focus of the ensemble was on the individual years of measurements (e.g., 2022 for winter) enabling avoiding the long-term variations (i.e., in decades) of ocean–sea ice feedbacks on the months of interest. This modelling design isolates the impact of the LAAs-induced heating by isolating a fast atmospheric response on a seasonal basis. The atmospheric response to the LAAs *HR* was evaluated by comparing the ensemble mean of the 140 sensitivity simulations with the control ones obtained in the same conditions avoiding the inclusion of LAAs *HR* data.

LAA *HR* was introduced within the PBL on the basis of the scientific questions reported in Section 1. Previous experimental campaigns along vertical profiles (both at midlatitudes and within the Arctic) showed quite homogeneous BC and *HR* values from the surface within the PBL for a vast majority of collected data both in the Arctic (>80% of cases) and at midlatitudes (quite all cases) [28,30,64]; similar results has been also shown in other literature researches [67,100–107] making reliable the approach for CESM2 sensitivity experiments; finally, MERRA-2 BC concentrations were only 3.2 ± 0.2 and 4.3 ± 0.4% (summer and winter) above the PBL compared to the ones within it.

The LAAs *HR* forcing input was introduced from midlatitudes till the north pole (40–90° N) during both June–July–August (summer) and February (winter); this choice has been done to model the same periods of time corresponding to the experimental ship-based LAAs measurements. The focus of the ensemble was on the individual years of measurements (e.g., 2022 for winter) enabling avoiding the long-term variations (i.e., in decades) of ocean–sea ice feedbacks on the months of interest.

This modelling design isolates the impact of the LAAs-induced heating while preserving interannual variability [108] as it is appropriate for isolating a fast atmospheric response on a seasonal basis, avoiding the capture of coupled ocean–sea ice feedbacks and isolating the rapid atmosphere–land changes (excluding the multi-year ocean and sea ice feedbacks); the design provides a process-based simulation of whether such an LAAs *HR* can modify the AMHT and the Arctic atmospheric temperature response. In fact, prescribed-forcing and fixed sea surface temperature experiments are established tools for diagnosing rapid atmospheric adjustments, including responses to absorbing aerosols [109,110]. The LAAs *HR* fixed the magnitude and spatial pattern of the heating perturbation, while CAM6 dynamics, turbulence and vertical mixing, convection, clouds, radiation, precipitation, hydrology and surface exchange remained interactive and responded to the imposed *HR*; most importantly, energy conservation constrained the complete atmospheric energy budget, therefore not requiring a particular poleward transport anomaly. In fact, CAM6 vertical mixing remains active and redistributes the temperature, humidity, and moist-static-energy response; cloud-radiative adjustments also remain active: CAM6 continues to calculate interactive clouds and radiative fluxes that respond to the imposed tendency. Therefore, any AMHTs anomaly is the result of the full atmospheric energy budget, including other adjustment mechanisms such as atmospheric energy storage, radiative adjustment, surface exchange, and horizontal energy divergence.

What is not considered is the long-term historical impact of LAAs, which is explicitly reserved for future emissions-driven, fully coupled simulations, which also require coupled ocean–sea ice feedbacks.

CESM2 data allowed the determination of the impact of LAAs *HR* on Arctic temperatures and the computation of AMHT during summer and winter (both for LAAs perturbed computation and for control simulations) following Fajber et al. [111]:

$$AMHT_{w/o-LAAs}(\theta_{Arc}) = 2\pi a^2 \int_{-\pi/2}^{\theta_{Arc}} Q_{TOT} \cos\theta \, d\theta \quad (16)$$

where Q_{TOT} is the difference between the net radiation at the top of the atmosphere and the sum of the total energy flux at the surface and the atmospheric storage, a is the Earth's radius, θ is the latitude and θ_{Arc} represents the 70° N Arctic boundary. Therefore, $AMHT(\theta_{Arc})$ reflects the northward flow of energy needed to balance the net loss of energy north of that latitude. Finally, the indices *w/o-LAAs* refer to the modelled atmospheric conditions with and without LAAs *HR* perturbation (i.e., perturbed and control conditions). $AMHT_{w\text{-}LAA}$ and $AMHT_{wo\text{-}LAA}$ allowed the determination of their difference, representing the energy transport induced by the presence of LAAs, hereinafter reported as $\Delta AMHT$ [112].

3. Results

The results are reported below for the ship-borne experimental data (Section 3.1), the large-scale structure MERRA-2 LAAs *HR* (Section 3.2) and CESM2 simulations (Section 3.3). All the data are reported as means ± confidence intervals at 95% probability.

3.1. Experimental Meridional Gradients in LAAs, Radiation and Heating Rate

LAAs concentrations were measured during the summer and winter campaigns and are expressed in terms of MeBC (Section 2.1). A consistent latitudinal decrease in MeBC in both seasons (Figures 2 and 3; Tables S1 and S2, and Figures S6 and S7 on a logarithmic scale in Supplementary Materials) was present. In summer (AREX campaigns, Figure 2), MeBC decreased from 751 ± 11 ng m^{-3} (Europe, Gdansk; 54° N) to 7 ± 1 ng m^{-3} in the northernmost Arctic region, aligning with previous literature values [22,23,113–115]. Intermediate MeBC values were observed in the Baltic-North Sea (169 ± 14 ng m^{-3}), North Sea (31 ± 3 ng m^{-3}) and the Barents Sea (between Trømso and the Svalbard Islands: 16 ± 2 ng m^{-3}). In winter, the BALTIC campaign data (Figure 3) indicated a similar trend, with MeBC decreasing from 921 ± 27 ng m^{-3} in Gdansk to 10–14 ± 1 ng m^{-3} in the Bothnia Gulf (62–63° N) until sea ice prevented further northward navigation.

As a consequence, $b_{abs}(\lambda)$ also experienced a similar decrease with latitude; in this respect, as detailed in Section 2.2, a proper latitudinal trend of $b_{abs}(\lambda)$ was obtained through the use of a dedicated latitudinal value of C_{AE} (Tables S1 and S2, Supplementary Materials). It is noteworthy that the multiple-scattering correction parameter C_{AE} showed an increase from the Baltic area (2.58 ± 0.03) through the North Sea (3.48 ± 0.07) and the Barents Sea (3.73 ± 0.08) to the open Arctic Ocean (5.91 ± 0.32, 80° N) as a consequence of the rise in the SSA_{AE} (470 nm) from 0.779 ± 0.007 (Baltic area), 0.884 ± 0.004 (North Sea), 0.898 ± 0.004 (Barents Sea) to 0.950 ± 0.004, 80° N (open Arctic Ocean).

The LAAs *HR* was assessed by coupling $b_{abs}(\lambda)$ with the impinging radiation (Equation (1)); therefore, the global shortwave irradiance trend is summarized below. It decreased during summer from 308 ± 4 W m^{-2} at Gdansk (54° N) to a range of 70 ± 3–158 ± 3 W m^{-2} across the Arctic (>70° N) (Figures 2 and S6), while the diffuse radiation fraction increased from 39.5 ± 0.5% to 75.7 ± 0.6% of the total, driven by greater cloud cover (3.99 ± 0.04 to 6.28 ± 0.02 oktas; Figure S6). This northward increase in diffuse radiation (the amount of solar radiation that is scattered in any direction by the air masses present in the sky and by the clouds) reflected enhanced atmospheric radiation scattering under cloudier Arctic conditions. In winter (Figures 3 and S7), the global shortwave radiation ranged from 64 ± 4 to 146 ± 4 W m^{-2} in the Baltic Sea, with no clear pattern of cloudiness, leading to a higher contribution of diffuse radiation in the Gdansk-south Baltic area due to greater cloud coverage (4.86 ± 0.32 oktas) compared with the Bothnia Gulf (1.97 ± 0.13 oktas), and with an average value of 93 ± 2 W m^{-2}; in the Arctic, shortwave radiation was essentially absent during winter.

LAAs and the available shortwave radiation determined (Equation (1), Section 2.1) the latitudinal trend of the LAAs *HR* in both summer and winter (Figures 2 and 3); it is noteworthy that the obtained *HR* is experimental and was assessed in all-sky conditions.

The *HR* values decreased from 335.5 ± 6.6 mK d^{-1} in Gdansk during summer and 254.0 ± 17.4 mK d^{-1} during winter to 0.9 ± 0.1 mK d^{-1} in the northernmost Arctic during summer, approaching zero in winter under polar-night conditions because of the absence of shortwave radiation. Intermediate *HR* values in summer were 85.0 ± 9.5 mK d^{-1} in the Baltic-North Sea, 7.0 ± 1.0 mK d^{-1} in the Norwegian Sea, and 2.4 ± 1.6 mK d^{-1} in the Arctic Ocean between Trømso and the islands of the Svalbard Archipelago.

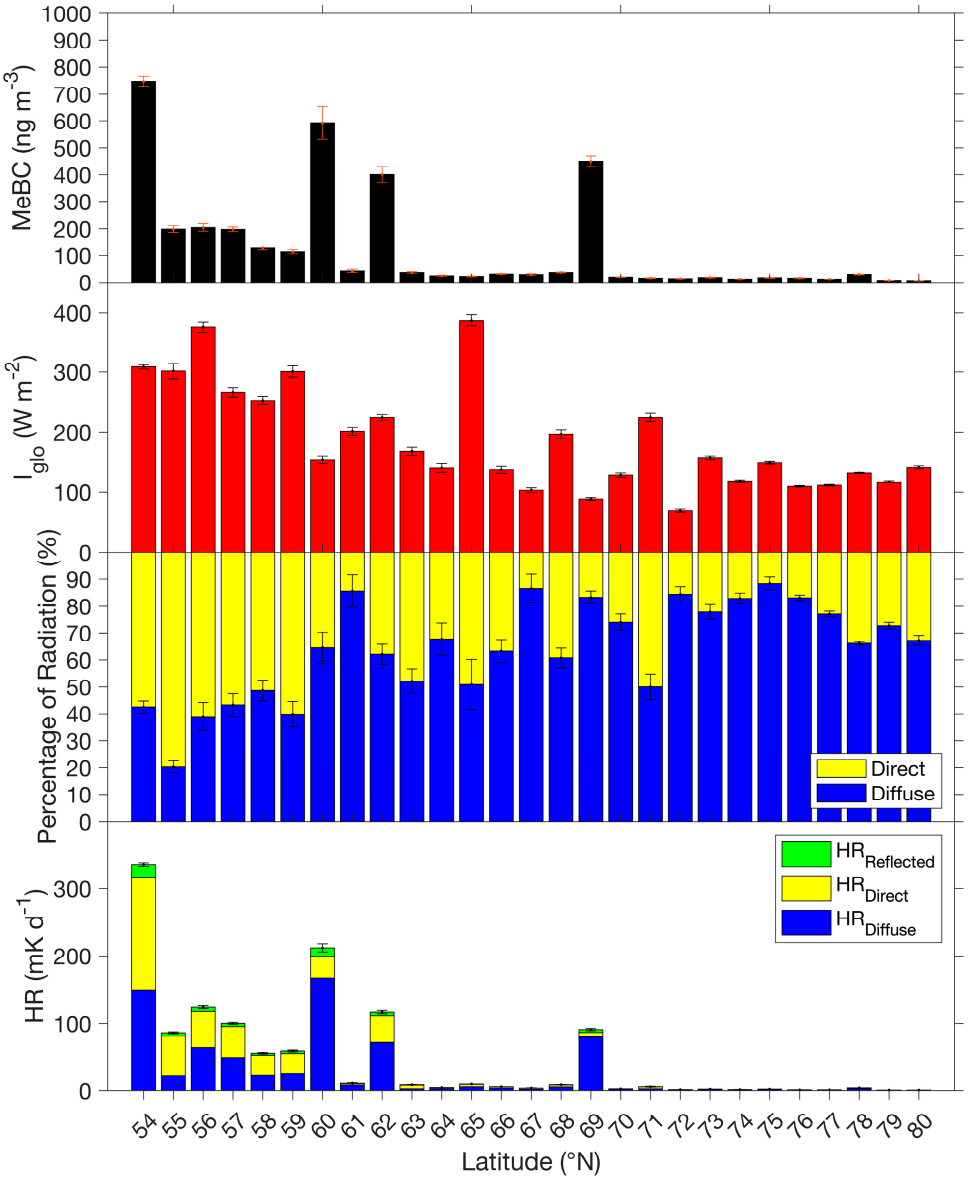


Figure 2. Latitudinal mean values of median equivalent-BC (MeBC), global irradiance (I_{glo}), percentage of direct and diffuse radiation in the global irradiance and the corresponding *HR* values divided into their direct, diffuse and reflected components (HR_{dir}, HR_{dif} and HR_{ref}) assessed during the summertime AREX campaigns. Error bars represent the confidence interval at 95% probability.

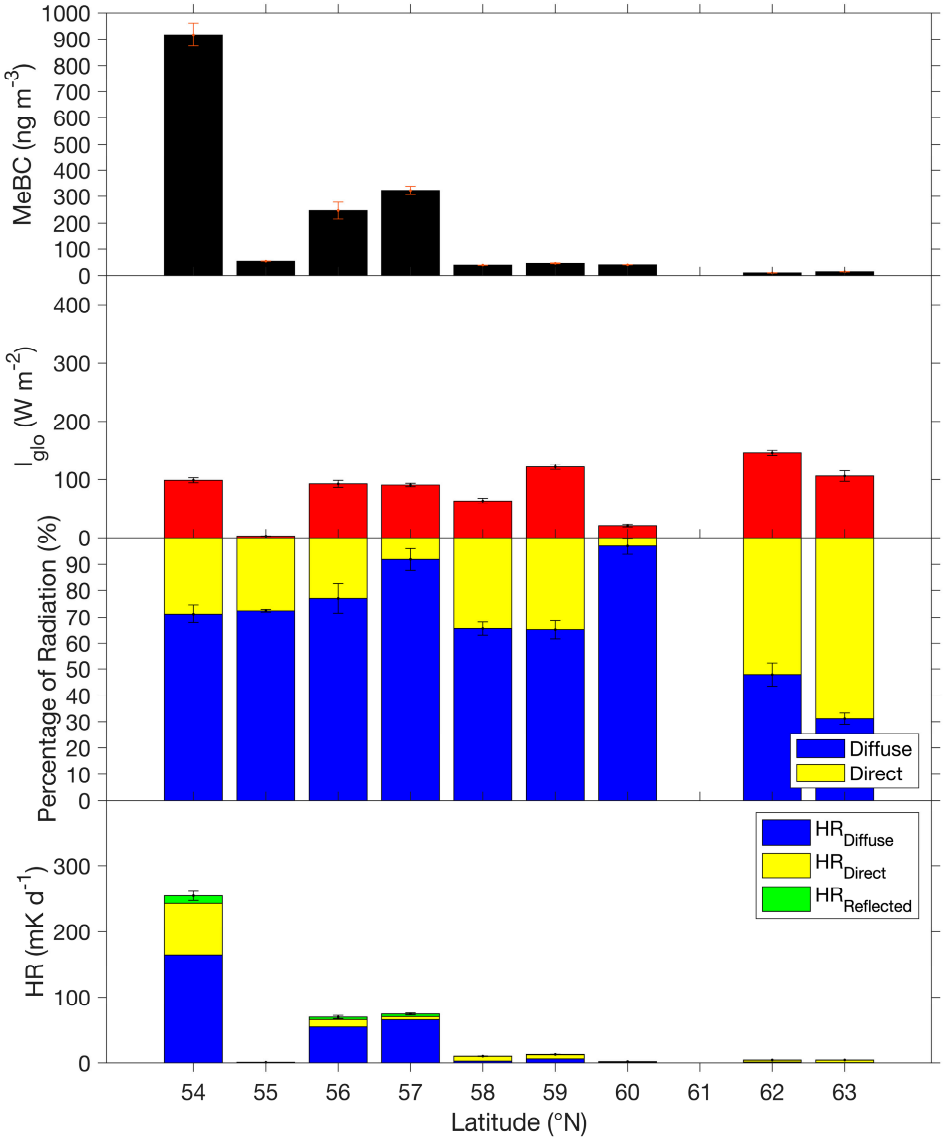


Figure 3. Latitudinal mean values of median equivalent-BC (MeBC), global irradiance (I_{glo}), percentages of direct and diffuse radiation in the global irradiance and the corresponding *HR* values divided into their direct, diffuse and reflected components (HR_{dir}, HR_{dif} and HR_{ref}) assessed during the wintertime BALTIC campaign. Error bars represent the confidence interval at 95% probability.

Finally, local MeBC and *HR* peaks occurred mostly in summer near human settlements: Bergen (MeBC: 595 ± 38 ng m^{-3}; *HR*: 212.3 ± 15.7 mK d^{-1}), Faroe Islands (MeBC: 403 ± 19 ng m^{-3}; *HR*: 116.8 ± 6.7 mK d^{-1}), Tromsø (MeBC: 453 ± 12 ng m^{-3}; *HR*: 90.7 ± 4.4 mK d^{-1}), and Longyearbyen (MeBC: 30 ± 1 ng m^{-3}; *HR*: 4.2 ± 0.1 mK d^{-1}). These localized increases were discussed in previous works; for example, Losi et al. [71] showed that the whole aerosol chemical composition highlighted substantial differences between the background Arctic Ocean and the anthropized settlements there, especially in terms of BC, which can locally account for up to ~20% of aerosol mass, being accompanied by an increase in the non-sea salt sulphate mass. Further, Ferrero et al. [27] showed that the contribution of long-range transported aerosol can raise the BC concentrations, after dispersion over the wide ocean, by a factor of ~10 ng m^{-3}, which is negligible compared to the huge and abrupt increase in MeBC values reported above for human settlements. Finally,

Cappelletti et al. [30] measured summertime eBC concentrations along vertical profiles over Longyearbyen (110 ± 10 ng m^{-3}) ~100 times higher than those found along vertical profiles in summer by Ferrero et al. [28] at the less anthropized site of Ny-Ålesund; only the arrival of tourist cruise ships enabled an impact on the atmospheric column in Ny-Ålesund similar to that observed in Longyearbyen. All these past data and those reported in the present work for human settlements suggest that local heating due to LAA may intensify in the near future as Arctic ice retreat expands the possibilities for human activities, as reported in Losi et al. [71].

Despite these local effects, the dominant pattern is a strong meridional gradient. Midlatitude MeBC concentrations and related *HR* values exceed Arctic values by a factor of ~400 during summer and even more in winter, producing greater atmospheric energy input at midlatitudes than in the Arctic. The LAAs *HR* enabled the determination of the daily atmospheric power surplus (*APS*, Figure 4) available in the atmosphere. In Gdansk, during summer and winter, LAAs contributed with *APS* values of 286.8 ± 0.1 and 227.4 ± 0.2 J d^{-1} m^{-3}, respectively. Conversely, in the Arctic during summer (at 80° N) and near the Arctic Circle during winter (Bothnia Gulf, 63° N), *APS* values were significantly lower, amounting to only 1.2 ± 0.1 and 4.7 ± 0.1 J d^{-1} m^{-3}, respectively. Of course, under polar-night conditions, *APS* was zero due to the absence of sunlight.

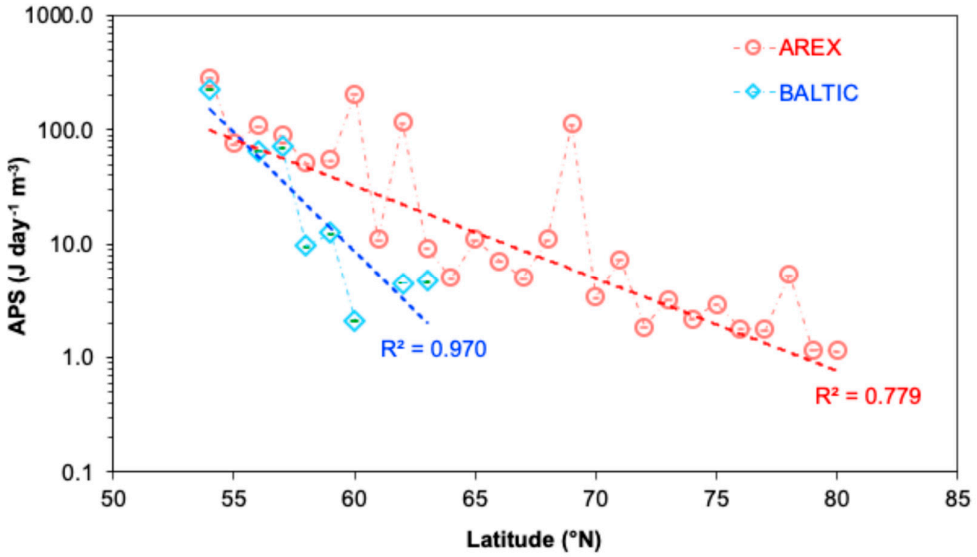


Figure 4. Latitudinal mean measured values of APS assessed during the AREX and BALTIC campaigns.

The latitudinal gradient of *APS* exhibited intermediate values across various regions during summertime, such as in the Baltic–North Sea, Norwegian Sea, and the Arctic Ocean (between Trømso and the Svalbard Islands), with *APS* values of 76.2 ± 0.1, 8.0 ± 0.1, and 3.1 ± 0.1 J d^{-1} m^{-3}, respectively. Local peaks of *APS* mirrored those of LAAs *HR*, as depicted in Figure 3. In wintertime, the mean *APS* within the Baltic (south of the Bothnia Gulf) was 39.6 ± 0.1 J d^{-1} m^{-3}.

APS exhibited an exponential latitudinal decrease with $R^2 > 0.77$; decay constants: −0.19 $degree^{-1}$ in summer (neglecting anthropic settlement spikes; see the previous section) and −0.44 $degree^{-1}$ in winter. This feature reflects both the spatial spread of LAAs from source regions (e.g., Europe) due to wind-driven natural dispersion and the relatively short lifetime of LAAs in the atmosphere (~ a couple of weeks) due to both wet and dry deposition processes [84,116]; as a result, on the wide hemispherical spatial scale (not local) LAAs are characterized by significant spatial variations with an heterogenous patter

(see also Sections 3.2 and 3.3) and sharp decrease towards the north due to the increasing distance from source regions.

This energy input described by *APS* can be stored temporarily or redistributed, and it can also be removed through radiation and surface exchange; a part can be transported to the Arctic via atmospheric circulation. In the simulations (Section 3.3), the Arctic warms more, compared to a scenario without LAAs forcing, due to the instantaneous amount of energy released at midlatitudes, which is subsequently transported (Section 3.3). Therefore, even if large human settlements exert a local impact (Figures 2 and 3), the atmospheric heat transport is subject to the dominating midlatitude–Arctic regional context, as detailed in Section 3.3.

3.2. Large-Scale Structure of the LAAs Heating Rate

CESM2 simulations cannot be computed using just a ship-based trajectory of LAAs *HR* input. As a consequence, the large-scale structure of the LAAs HR was based on the experimentally driven *HR* spatial data obtained from MERRA-2.

As reported in Section 2.3.2, an empirical environmental MAC (*eMAC*) was needed and computed following Equation (15). This computation resulted in an average *eMAC* value of 8.7 ± 0.1 m^2 g^{-1} in summer and 12.7 ± 0.3 m^2 g^{-1} in winter; the obtained *eMAC* empirically embedded both the approximation introduced in Equation (14) and the small fraction of *ADRE* due to species other than BC.

Figure 5a,b show the latitudinal changes of MERRA-2 BC, global irradiance in all-sky conditions (I_{glo}), albedo and obtained *HR* (Equation (14)) while Figure 6 shows the corresponding polar view of the computed *HR*. As Figure 5a,b show, MERRA-2 BC concentrations decreased latitudinally as observed during the ship-borne campaigns. In summer, BC decreased from 362 ± 6 ng m^{-3} (40–55° N) to 173 ± 11 ng m^{-3} (55–70° N) and then to 94 ± 1 ng m^{-3} north of 70° N. In winter, the highest BC concentrations were found close to 40° N (up to ~400 ng m^{-3}) rapidly decreasing to 138 ± 2 ng m^{-3} (40–55° N), to 37 ± 1 ng m^{-3} (55–70° N) and then to 34 ± 1 ng m^{-3} north of 70° N. Different phenomena can be at the base of such values, and as stated in Section 2.3, the intent is not to validate MERRA-2; we only underline that the Arctic values are higher than the ship-borne MeBC measurements and then those reported in the literature [22,23,113–115]. Remarkably, the LAAs *HR* is obtained by combining BC concentrations with radiation and the previous *eMAC* values. As a result, the lower Arctic irradiance reduced the absolute *HR* associated with MERRA-2 BC values in the Arctic. In particular, I_{glo} decreased northward in both seasons from 220 ± 1 W m^{-2} (summer) and 60 ± 1 W m^{-2} (winter) at 40–55° N, to 187 ± 2 W m^{-2} (summer) and 11 ± 1 W m^{-2} (winter) between 55° and 70° N and then to 181 ± 1 W m^{-2} (summer) and ~zero (winter) north of 70° N. Albedo, instead, increased in both seasons (higher in winter than summer) driven by sea ice and the Greenland ice sheet.

The combined decrease in BC and solar irradiance produced a sharper *HR* gradient than that of only BC alone; in fact, in summer, the *HR* decreased from 152.4 ± 2.2 (40–55° N) and 38.1 ± 2.4 (55–70° N) mK d^{-1} and then to 16.4 ± 0.2 mK d^{-1} in the Arctic area. The Arctic *HR* was just 11 ± 1% with respect to midlatitudes, while the Arctic BC of MERRA-2 was 26 ± 1% of the midlatitudes one. The winter *HR* had a sharper northward gradient, with values of 35.1 ± 0.8 (40–55° N) and 1.0 ± 0.1 (55–70° N) mK d^{-1}, decreasing to zero in the Arctic polar night, leading to a 0% of *HR* in the Arctic with respect to midlatitudes, while the BC was 25 ± 1%.

As shown in Figure 6, most of the *HR* signal came from land where BC sources are located. In fact, considering the land sector (Eurasia and America) in summer the *HR* decreased from 207.4 ± 3.3 (40–55° N) and 43.7 ± 3.8 (55–70° N) mK d^{-1} and then to 16.1 ± 0.3 mK d^{-1} in the Arctic, while over the oceanic sector (Atlantic and Pacific) the *HR* decreased from 59.7 ± 0.7 (40–55° N) to 28.7 ± 1.1 (55–70° N) mK d^{-1} and then to 17.0 ± 0.2 mK d^{-1} in

the Arctic; in winter, the corresponding *HR* values over land were 51.1 ± 1.3 (40–55° N) and 0.9 ± 0.1 (55–70° N) mK d^{-1}, decreasing to zero in the Arctic, while over oceans the *HR* was negligible, decreasing from 8.3 ± 0.1 (40–55° N) to 0.7 ± 0.1 (55–70° N) mK d^{-1} and then to zero in the Arctic (Figure S8 and S9, Supplementary Materials). With respect to this point, it is interesting to underline the summer case, when solar radiation is available at the North Pole. In summer, the Arctic-to-midlatitudes ratio for BC was 26.0 ± 0.5% while the same ratio for I_{glo} was 82.2 ± 0.2%. This was more evident comparing land and ocean gradients (Figures S8 and S9); focusing on the European sector, the Arctic-to-midlatitudes ratio for BC was 19.3 ± 0.4%, while the same ratio for I_{glo} was 72.8 ± 0.5%. Finally, as reported in Figures 5a, S8 and S9, the surface albedo was 3.5 times higher in the Arctic than at midlatitudes, being responsible for a higher contribution of I_{ref} on the LAAs *HR* in the Arctic. As a conclusion, summer data evidenced that the driving variable for the LAAs *HR* was the BC, leaving a minor contribution to all the irradiance terms (I_{glo} and I_{ref}) making any uncertainty in the MERRA-2 radiation data in all-sky conditions less important with respect to the BC behaviour.

Finally, it is noteworthy that, even if a direct comparison of *HR* is not possible on a global scale due to the large spatial scale of the MERRA-2 data, they were checked along the ship track; in the Gulf of Gdansk, the *HR* values were 255.1 ± 11.3 mK d^{-1} during summer and 107.6 ± 21.1 mK d^{-1} during winter, decreasing to 7.3 ± 0.1 mK d^{-1} in the northernmost Arctic during summer and to zero in winter. Intermediate *HR* values in summer were 74.7 ± 21.8 mK d^{-1} in the North Sea and 9.3 ± 0.5 mK d^{-1} in the Norwegian Sea, showing a broadly similar latitudinal pattern to the experimental data reported in Section 3.1.

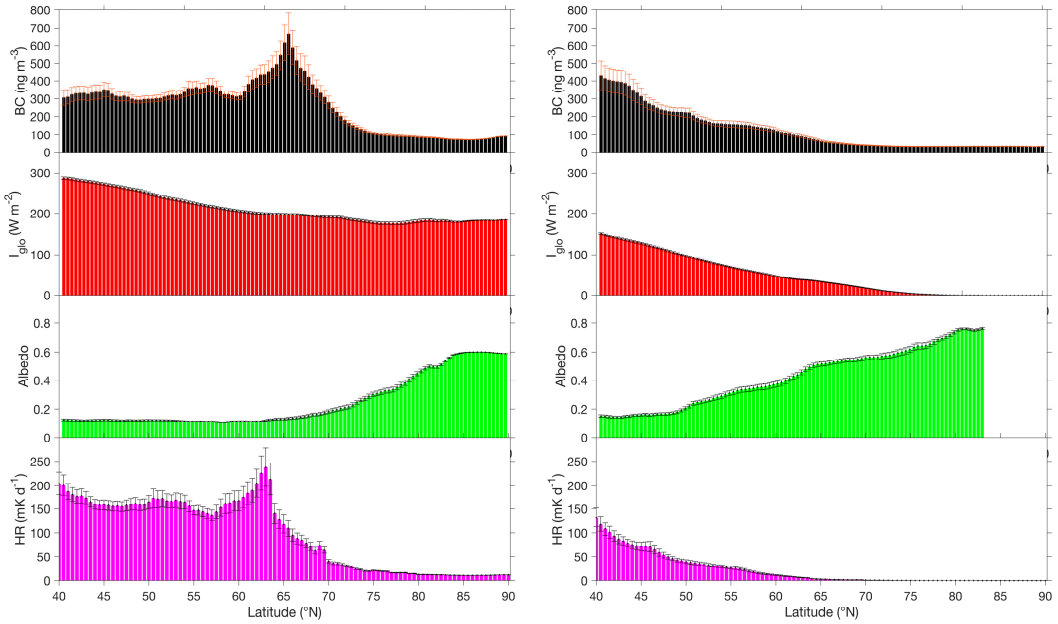


Figure 5. Latitudinal mean values of MERRA-2 black carbon (BC), global irradiance (I_{glo}), albedo and heating rate (*HR*) values for summer (**a**) and winter (**b**). Error bars represent the confidence interval at 95% probability.

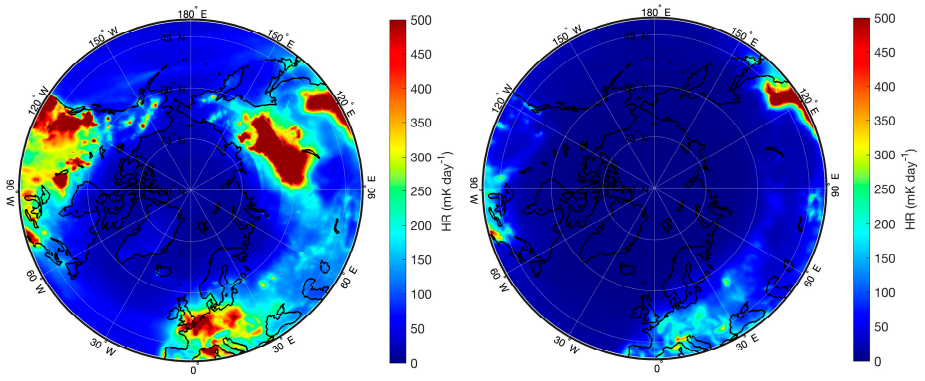


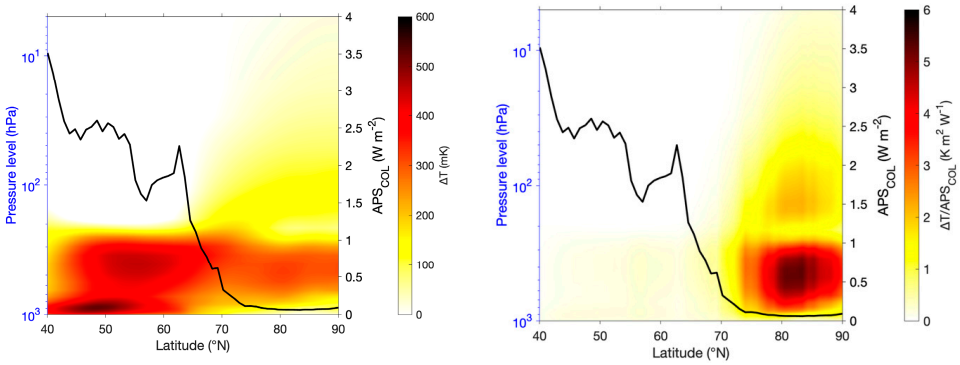
Figure 6. Summertime and wintertime LAAs *HR* in panels (**a**) and (**b**), respectively.

3.3. Observationally Driven Model Response

The LAAs *HR* reported in Figure 6 was applied to the American NCAR CESM v2.2 modelling system in perturbed simulations over 140 ensembles, enabling a comparison of the results with and without LAAs *HR* (Section 2.4). In this respect, all the CESM2 data are reported as means ± confidence intervals at 95% probability, considering the variability generated by the 140 ensemble pairs.

The vertical meridional cross-section of the CESM2 results, in terms of a ΔT (perturbed vs. control simulations), for both summer and winter, is reported in Figure 7a–d together with the APS_{COL} (Section 2.3). From Figure 7a–d, it is clear that the LAAs *HR* induced small but systematic warming of the Arctic atmospheric column.

Figure 7a shows that in summer, the columnar Arctic ΔT was 100.2 ± 0.1 mK, double than the midlatitudes ΔT of 54.2 ± 0.2 mK and higher than the global one of 90.7 ± 0.2 mK, leading to a LAAs-induced Arctic-to-global temperature response ratio of 1.1; it is noteworthy that, despite the fact that AA is defined as a ratio of warming trends, the obtained Arctic-to-global temperature is close to that expected, even if it should be distinguished from the summertime surface-warming trend ratio reported in Rantanen et al. [1].



https://doi.org/10.3390/earth7060187

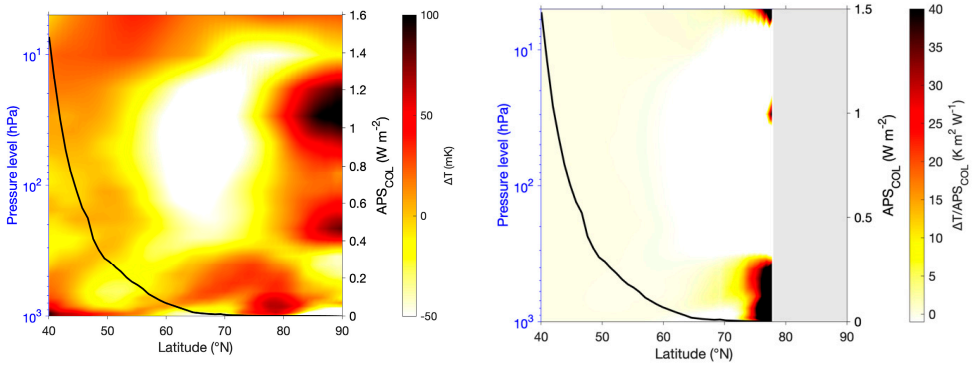


Figure 7. Meridional vertical cross-sections of temperature increase (in mK; panels (**a**,**c**)) and temperature increase per unit LAAs-*APS* forcing (in K m² W⁻¹; panels (**b**,**d**)). The top panels (**a**,**b**) refer to the summer scenario, while the bottom ones (**c**,**d**) refer to the winter scenario. The black solid line represents the latitudinal behaviour of *APS*. Note that scales are season-dependent; this has been done to enhance figure clarity for both winter and summer, avoiding the use of a common scale that would suppress the possibility of clearly visualizing the spatial patterns of APS_{COL}, ΔT and $\Delta T/APS_{COL}$.

The vertical cross sections revealed distinct structures in the midlatitude and Arctic responses. In summer, midlatitude warming was concentrated near the surface and within the PBL (ΔT: 333.1 ± 5.4 mK), with a small net cooling above the troposphere, whereas in the Arctic the largest temperature increase (ΔT: 246.5 ± 1.4 mK) occurred within the troposphere and extended into the lower stratosphere, despite much less available energy (APS_{COL}); the corresponding global tropospheric ΔT was 111.8 ± 1.3 mK, half of that registered in the Arctic.

In winter (Figure 7c), the columnar Arctic ΔT was 7.2 ± 5.2 mK, higher than the midlatitude ΔT of −8.5 ± 3.6 mK, which was negative, while the global ΔT was −0.1 ± 0.9 mK, statistically lower than the Arctic one and also statistically indistinguishable from zero (indicating negligible global temperature change from LAAs forcing applied at 40° N and above); therefore, the corresponding LAAs-induced Arctic-to-global temperature response ratio cannot be determined. The imposed heating at midlatitudes was strongly confined within the PBL (ΔT: 28.1 ± 13.4 mK), yet the Arctic response emerged close to the ground and in the free troposphere (ΔT: 24.8 ± 4.5 mK) and above at high latitudes, consistent with poleward and upward redistribution of energy modulated by the polar dome [117,118].

The obtained results for both summer and winter are consistent with literature findings related to a tropospheric warming obtained with different approaches [119–121].

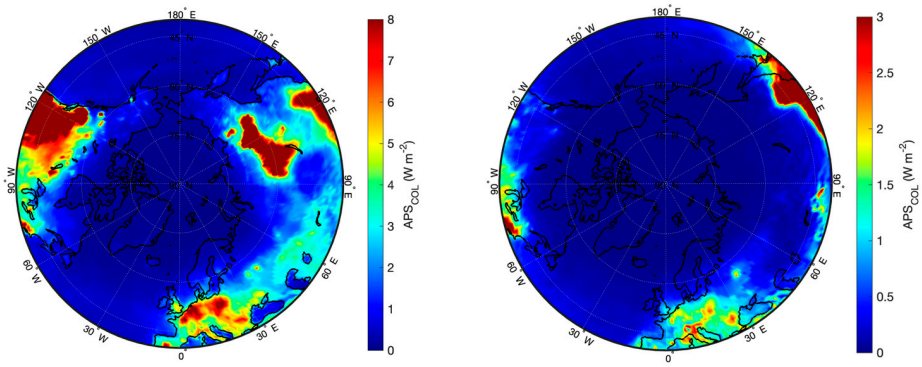
CESM2 outputs were also expressed as ΔT normalized by LAAs APS_{COL} (expressed in K m² W⁻¹) to highlight the ratio of ΔT with respect to the energy made locally available by the LAAs. In fact, if ΔT were only due to the local LAAs *HR*, $\Delta T/APS_{COL}$ should vary only due to atmospheric processes and/or local feedbacks.

APS_{COL} decreased northward (Figure 7), being 19 ± 1 times higher at midlatitudes than in the Arctic during summer (88.7% of APS_{COL} below 70° N) and 348 ± 21 times higher in winter (99.8% of APS_{COL} below 70° N). In summer, the Arctic $\Delta T/APS_{COL}$ was 0.948 ± 0.033 K m² W⁻¹, more than 30 times higher than at midlatitudes (0.027 ± 0.001 K m² W⁻¹); in winter, the Arctic $\Delta T/APS_{COL}$ reached 7.733 ± 5.673 K m² W⁻¹ (~73% uncertainty due to the heterogeneous spatial response of the Arctic region), ~300 times the magnitude of the midlatitude value (−0.026 ± 0.011 K m² W⁻¹). Therefore, the Arctic response per unit forcing

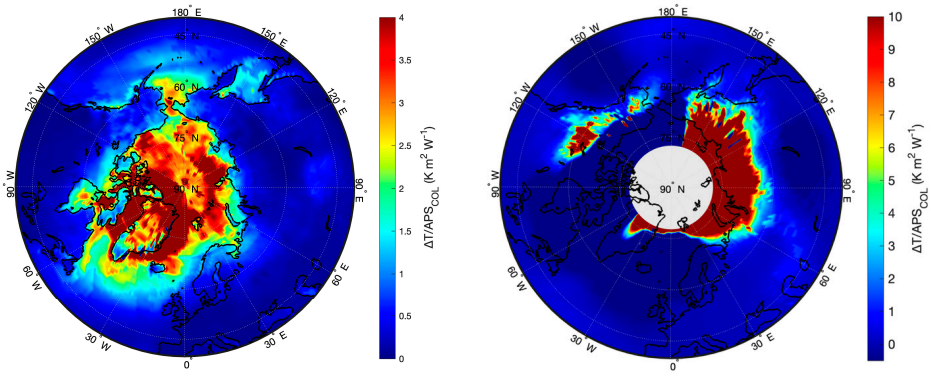
($\Delta T/APS_{COL}$) was always larger than at mid latitudes in both seasons by a factor of ten or more, as shown in Figure 7b,d and in the corresponding polar maps in Figure 8a–d. The large temperature-to-local-forcing ratio was especially evident in winter, when $\Delta T/APS_{COL}$ reached values well above 10 K m^2 W^{-1} (by a factor of 100 or more), becoming undefined where APS_{COL} is zero during the polar night. Given this, the purpose of the normalization of ΔT with respect to APS_{COL} was precisely to highlight the spatial disparities that increase toward the Arctic. In fact, if ΔT were only due to the local LAAs *HR*, $\Delta T/APS_{COL}$ should vary only due to atmospheric processes and/or local feedbacks. For example, in winter, the effect of atmospheric heating due to LAAs in the Arctic was negligible, while ΔT was positive and disproportionate with respect to the local heating forcing, therefore suggesting the role of other processes, such as the atmospheric meridional heat transport. This is in keeping with the findings suggested by Fajber et al. [117].

To interpret the previous Arctic ΔT and $\Delta T/APS_{COL}$, both $AMHT_{w\text{-}LAAs}$ and $AMHT_{wo\text{-}LAAs}$ (the *w*/*wo*-*LAA* notations refer to the modelled atmospheric conditions with and without the LAA aerosol effect, respectively) were computed from CESM2 output (Equation (16)) allowing the determination of their difference, referred to here as $\Delta AMHT$. $\Delta AMHT$ enabled us to account for the northward heat transport solely due to the induced perturbation, showing an atmospheric poleward energy transport of 7 ± 2 to 5 ± 1 TW (summer and winter, respectively), representing the dynamical pathway by which a fraction of this surplus is transported towards higher latitudes via the so-called lateral energy export, in agreement with the observations of Fajber et al. [117], who describe how midlatitude thermal perturbations close to the surface can drive a temperature response in the Arctic midtroposphere.

We underline here that the aforementioned results refer only to: (1) the seasons under investigation through experimental measurements; (2) the LAA contribution alone. It is noteworthy that, even if this mechanism alone cannot account for all the multidecadal Arctic surface warming since 1979 [1], the obtained results demonstrated that the LAA forcing can influence Arctic warming. These process-level results are consistent with the broader evidence supporting reductions in LAAs emissions as a near-term complement to long-lived greenhouse-gas mitigation (Section 4).



(**a**) (**b**)



(**c**) (**d**)

Figure 8. Summertime and wintertime LAAs-APS_{COL} forcing in panels (**a**,**b**), respectively. Corresponding temperature increase per unit LAAs-APS_{COL} forcing (ΔT in K m^2 W^{-1}) for (**c**) summer and (**d**) winter within the troposphere. Note that scales are season-dependent; this has been done to enhance figure clarity for both winter and summer, avoiding the use of a common scale that would suppress the possibility of clearly visualizing the spatial patterns of both APS_{COL} and $\Delta T/APS_{COL}$.

4. Discussion

The first observational quantification of the LAAs-induced *HR* gradient from midlatitudes to the Arctic (Section 3) goes in the same direction as model predictions [45] showing that remote LAA forcing can affect the Arctic via poleward energy transport. This mechanism—midlatitude heat release and poleward transport—explains why Arctic temperature responses exceed midlatitude responses despite lower local Arctic forcing, leading to an Arctic-to-global temperature response ratio higher than one.

Leading to an Arctic increase in temperature, LAAs have the potential to further influence other inner Arctic feedbacks, such as the reduction in snow and ice cover, leading to non-linear effects. This reduction decreases albedo and impacts ocean–atmosphere gas exchange and aerosol precursor emissions [7,10–12], which in turn influence the changes in cloud cover and related feedbacks; these feedback mechanisms are mostly positive in winter and negative in summer, adding complexity to the understanding of AA dynamics [7,8,13]. The enhanced Arctic warming can also weaken the meridional (equator-to-pole) temperature gradient, potentially decreasing atmospheric dry static energy transport [14,48], while increasing the energy associated with moisture increase [6,14,122]. However, the same AA can affect the large-scale circulation in the midlatitudes [43,123], such as the poleward-propagating synoptic waves [124–127] and the northward shift of the Intertropical Convergence Zone [122], thereby increasing the meridional transport of both heat and moisture. We underline that all the aforementioned mechanisms are of general interest for the Arctic area and all of them should be influenced by a LAAs-induced AMHT, making this possible connection a target for future studies.

Historical trends in aerosol emissions reveal a notable decrease in atmospheric sulphur content at midlatitudes in Europe and North America, primarily due to health-related policies, while black carbon (BC) concentrations have shown varied trends over time [128,129]. As a result, the multidecadal trend of the aerosol scattering coefficient has been negative in Europe and North America (not statistically significant in Asia) [83]. In contrast, the absorption coefficient, largely influenced by LAAs like BC, has exhibited both declining and increasing trends [83]; this dynamic interplay affects the single-scattering albedo trend, with positive trends predominant in Asia and eastern Europe, and negative trends in western Europe [21] and North America. This suggests that historical pollutant

abatement measures, such as those implemented in western Europe during the 1980s, have contributed to a present-day decrease in the single-scattering albedo trend in the Western Hemisphere [83]. As reported in the literature, changes in aerosol emissions at midlatitudes or in the tropics can influence the Arctic region [54], indicating that future studies should further investigate the impact of policies, aimed at mitigating LAA at midlatitudes, as short-term climate strategies [13,130,131] with respect to Arctic warming.

5. Conclusions

We provided the first observational ship-borne quantification of the LAAs-induced *HR* gradient from midlatitudes to the Arctic, showing that it declined from 335.5 ± 6.6 mK d^{-1} in summer and 254.0 ± 17.4 mK d^{-1} in winter, near Europe, to 0.9 ± 0.1 mK d^{-1} in summer with zero HR inferred in winter under polar-night conditions. As a result, the atmospheric power surplus differed by more than two orders of magnitude between midlatitudes and the Arctic.

A new methodology was developed to use reanalysis data (in the present work, MERRA-2) to determine the LAAs *HR* on a global scale, and it was applied to the Northern Hemisphere, from midlatitudes to the Arctic. Results broadly reproduced the latitudinal pattern of the ship-borne observations and were used as input for CESM2 applied in the single-model initial-condition large-ensemble approach (SMILE).

Up to now, the role of LAAs in Arctic amplification has remained poorly constrained from the observations. Therefore, in the present work, we combined the experimental data with reanalysis data (MERRA-2) to derive a reanalysis *HR* field constrained by shipborne observations to drive climate model simulations (CESM2) assessing how the meridional gradients in LAAs *HR* can influence Arctic warming. Results showed that LAAs-induced atmospheric heating enhanced poleward atmospheric meridional heat transport by 7 ± 2 and 5 ± 1 TW (in summer and in winter), leading to a seasonal Arctic-to-global temperature ratio of 1.1 in summer and a ratio that was not meaningfully defined in winter, as the Arctic warmed, while the global temperature response was statistically indistinguishable from zero.

Further cruises and research will be required in the future to deepen our understanding of this process and related LAAs sources across the Northern Hemisphere.

Supplementary Materials: The following supporting information can be downloaded at https://www.mdpi.com/article/10.3390/earth7060187/s1. Figure S1. Research vessel Oceania, operated by the Institute of Oceanology, Polish Academy of Sciences. Figure S2. Outward and return cruise paths during the three summer ARctic EXpeditions (AREX: 2018, 2019, 2021; panels: a–c) and the winter BALTIC campaign (2022) (panel d). Red dots indicate the main human settlement hot spots present along the cruises. Table S1. Latitudinal mean values of median equivalent-BC (MeBC) and the corresponding heating rate (*HR*), Absorptive Direct Radiative Forcing (*ADRE*) and multiple-scattering correction factor C_{AE} assessed during the summertime AREX campaigns. Table S2. Latitudinal mean values of Median equivalent-BC (MeBC) and the corresponding heating rate (*HR*), Absorptive Direct Radiative Forcing (*ADRE*) and the multiple-scattering correction factor C_{AE} assessed during the wintertime BALTIC campaign. Figure S3. Percentage of BC and BrC along AREX (a) and BALTIC (b) cruises. Figure S4. Percentage of each okta of cloudiness depending on the location during the AREX cruises. Figure S5. Percentage of each okta of cloudiness depending on the location during the BALTIC cruise. Figure S6. Latitudinal mean values of median equivalent-BC (MeBC), global irradiance (I_{glo}), percentage of direct and diffuse radiation in the global irradiance and the corresponding *HR* values divided into their direct, diffuse and reflected components (HR_{dir}, HR_{dif} and HR_{ref}) assessed during the summertime AREX campaigns. Error bars represent the confidence interval at 95% probability. Figure S7. Latitudinal mean values of median equivalent-BC (MeBC), global irradiance (I_{glo}), percentage of direct and diffuse radiation in the global irradiance

and the corresponding *HR* values divided into their direct, diffuse and reflected components (HR_{dir}, HR_{dif} and HR_{ref}) assessed during the wintertime BALTIC campaign. Error bars represent the confidence interval at 95% probability. Figure S8. Latitudinal mean values of MERRA-2 black carbon (BC), global irradiance (I_{glo}), albedo and heating rate (*HR*) values for summer (a) and winter (b) over the land sectors (Eurasia and America). Error bars represent the confidence interval at 95% probability. Figure S9. Latitudinal mean values of MERRA-2 black carbon (BC), global irradiance (I_{glo}), albedo and heating rate (*HR*) values for summer (a) and winter (b) over the ocean sectors (Atlantic and Pacific). Error bars represent the confidence interval at 95% probability.

Author Contributions: Conceptualization, L.F., T.Z. and E.B.; methodology, L.F., G.M. and N.L.; software, L.F., N.L., A.R., M.K. and Y.-B.Z.; validation, L.F., A.R., M.K. and Y.-B.Z.; formal analysis, L.F., M.K., A.R. and Y.-B.Z.; experimental campaigns, N.L., L.F., P.M. (Piotr Markuszewski) and P.M. (Przemysław Makuch) resources, G.M., M.R., A.G., V.D., E.B., L.F. and T.Z.; data curation, L.F., A.R., M.K., G.M., A.D. and Y.-B.Z.; writing—original draft preparation, L.F.; writing—review and editing, All authors. All authors have read and agreed to the published version of the manuscript.

Funding: This research was partially founded by the project GAIA (New Integrated Experimental and Modelling Tools for Georeferenced Source Apportionment of Aerosol Climate-Relevant Parameters from the Mediterranean Area to the Arctic) Project PRIN2022 MUR, Funded by European Union—Next Generation EU and by the project MUR TECLA "Dipartimenti di Eccellenza 2023–2027".

Data Availability Statement: Experimental data and HR codes are available on Zenodo at https://doi.org/10.5281/zenodo.12743871. CESMv2.2 simulations can be found at https://doi.org/10.5281/zenodo.17363758. MERRA 2 data are available at https://gmao.gsfc.nasa.gov/gmao-products/merra-2/data-access_merra-2/ (accessed on 30 October 2026).

Acknowledgments: This work is an output of (1) The project GAIA (New Integrated Experimental and Modelling Tools for Georeferenced Source Apportionment of Aerosol Climate-Relevant Parameters from the Mediterranean Area to the Arctic) Project PRIN2022 MUR, Funded by European Union—Next Generation EU. (2) The GEMMA Center in the framework of project MUR TECLA "Dipartimenti di Eccellenza 2023–2027". This work is also an output and Slovenian Research Agency program P1-0385. This research was also supported by the National Science Center grant SMART (grant no. 2023/49/B/ST10/00513), and the Polish National Agency for Academic Exchange (grant no. BPN/BEK/2024/1/00044). The authors want to acknowledge Aerosol d.o.o and the Polish Academy of Sciences statutory activity for supporting the experimental campaigns. We kindly thank the crew of the r/v Oceania for all technical assistance and safety care during the cruise. We thank the German Climate Computing Center (DKRZ) for using its supercomputer Levante on which the CESM 2.2 simulations were conducted. Finally, the authors wish to express their gratitude to the Reviewers for the helpful comments concerning the first version of the paper.

Conflicts of Interest: M.R. and A.G. are employed by the aerosol instrument manufacturer Aerosol d.o.o., G.M. is partially employed and is a co-owner of the aerosol instrument manufacturer Haze Instruments d.o.o.

References

1. Rantanen, M.; Karpechko, A.Y.; Lipponen, A.; Nordling, K.; Hyvärinen, O.; Ruosteenoja, K.; Vihma, T.; Laaksonen, A. The Arctic has warmed nearly four times faster than the globe since 1979. *Commun. Earth Environ.* **2022**, *3*, 168.
2. Serreze, M.C.; Barry, R.G. Processes and impacts of Arctic amplification: A research synthesis. *Glob. Planet. Change* **2011**, *77*, 85–96.
3. Shindell, D.; Faluvegi, G. Climate response to regional radiative forcing during the twentieth century. *Nat. Geosci.* **2009**, *2*, 294–300.
4. England, M.R.; Eisenman, I.; Lutsko, N.J.; Wagner, T.J.W. The Recent Emergence of Arctic Amplification. *Geophys. Res. Lett.* **2021**, *48*, e2021GL094086.

5. Maturilli, M.; Herber, A.; König-langlo, G. Surface Radiation Climatology for Ny-Ålesund, Svalbard (78.9 °N), Basic Observations for Trend Detection. *Theor. Appl. Climatol.* **2015**, *120*, 331–339.
6. Previdi, M.; Smith, K.L.; Polvani, L.M. Arctic amplification of climate change: A review of underlying mechanisms. *Environ. Res. Lett.* **2021**, *16*, 093003.
7. Goosse, H.; Kay, J.E.; Armour, K.C.; Bodas-Salcedo, A.; Chepfer, H.; Docquier, D.; Jonko, A.; Kushner, P.J.; Lecomte, O.; Massonnet, F.; et al. Quantifying climate feedbacks in polar regions. *Nat. Commun.* **2018**, *9*, 1919.
8. Pithan, F.; Mauritsen, T. Arctic amplification dominated by temperature feedbacks in contemporary climate models. *Nat. Geosci.* **2014**, *7*, 181–184.
9. Bintanja, R.; Graversen, R.G.; Hazeleger, W. Arctic winter warming amplified by the thermal inversion and consequent low infrared cooling to space. *Nat. Geosci.* **2011**, *4*, 758–761.
10. Dai, A.; Luo, D.; Song, M.; Liu, J. Arctic amplification is caused by sea-ice loss under increasing CO_2. *Nat. Commun.* **2019**, *10*, 121.
11. Thackeray, C.W.; Hall, A. An emergent constraint on future Arctic sea-ice albedo feedback. *Nat. Clim. Change* **2019**, *9*, 972–978.
12. Dallósto, M.; Beddows, D.C.S.; Tunved, P.; Krejci, R.; Ström, J.; Hansson, H.C.; Yoon, Y.J.; Park, K.T.; Becagli, S.; Udisti, R.; et al. Arctic sea ice melt leads to atmospheric new particle formation. *Sci. Rep.* **2017**, *7*, 3318.
13. Quinn, P.K.; Bates, T.S.; Baum, E.; Doubleday, N.; Fiore, A.M.; Flanner, M.; Fridlind, A.; Garrett, T.J.; Koch, D.; Menon, S.; et al. Short-lived pollutants in the Arctic: Their climate impact and possible mitigation strategies. *Atmos. Chem. Phys.* **2008**, *8*, 1723–1735.
14. Hwang, Y.T.; Frierson, D.M.W.; Kay, J.E. Coupling between Arctic feedbacks and changes in poleward energy transport. *Geophys. Res. Lett.* **2011**, *38*, L17704.
15. Chemke, R.; Polvani, L.M.; Kay, J.E.; Orbe, C. Quantifying the role of ocean coupling in Arctic amplification and sea-ice loss over the 21st century. *npj Clim. Atmos. Sci.* **2021**, *4*, 46.
16. Zhang, P.; Chen, G.; Ting, M.; Ruby Leung, L.; Guan, B.; Li, L. More frequent atmospheric rivers slow the seasonal recovery of Arctic sea ice. *Nat. Clim. Change* **2023**, *13*, 266–273.
17. Graversen, R.G.; Burtu, M. Arctic amplification enhanced by latent energy transport of atmospheric planetary waves. *Q. J. R. Meteorol. Soc.* **2016**, *142*, 2046–2054.
18. Graversen, R.G.; Mauritsen, T.; Tjernström, M.; Källén, E.; Svensson, G. Vertical structure of recent Arctic warming. *Nature* **2008**, *451*, 53–56.
19. Gogoi, M.M.; Babu, S.S.; Moorthy, K.K.; Thakur, R.C.; Chaubey, J.P.; Nair, V.S. Aerosol black carbon over Svalbard regions of Arctic. *Polar Sci.* **2016**, *10*, 60–70.
20. Breider, T.J.; Mickley, L.J.; Jacob, D.J.; Ge, C.; Wang, J.; Sulprizio, M.P.; Croft, B.; Ridley, D.A.; McConnell, J.R.; Sharma, S.; et al. Multidecadal trends in aerosol radiative forcing over the Arctic: Contribution of changes in anthropogenic aerosol to Arctic warming since 1980. *J. Geophys. Res.* **2017**, *122*, 3573–3594.
21. Rovira, J.; Savadkoohi, M.; Chen, G.I.; Močnik, G.; Aas, W.; Alados-Arboledas, L.; Artiñano, B.; Aurela, M.; Backman, J.; Banerji, S.; et al. A European aerosol phenomenology—9: Light absorption properties of carbonaceous aerosol particles across surface Europe. *Environ. Int.* **2025**, *195*, 109185.
22. Eleftheriadis, K.; Vratolis, S.; Nyeki, S. Aerosol black carbon in the European Arctic: Measurements at Zeppelin station, Ny-Ålesund, Svalbard from 1998–2007. *Geophys. Res. Lett.* **2009**, *36*, L02809.
23. Popovicheva, O.B.; Evangeliou, N.; Kobelev, V.O.; Chichaeva, M.A.; Eleftheriadis, K.; Gregorič, A.; Kasimov, N.S. Siberian Arctic black carbon: Gas flaring and wildfire impact. *Atmos. Chem. Phys.* **2022**, *22*, 5983–6000.
24. Udisti, R.; Bazzano, A.; Becagli, S.; Bolzacchini, E.; Caiazzo, L.; Cappelletti, D.; Ferrero, L.; Frosini, D.; Giardi, F.; Grotti, M.; et al. Sulfate source apportionment in the Ny-Ålesund (Svalbard Islands) Arctic aerosol. *Rendiconti Lincei* **2016**, *27*, 85–94.
25. Lupi, A.; Busetto, M.; Becagli, S.; Giardi, F.; Lanconelli, C.; Mazzola, M.; Udisti, R.; Hansson, H.C.; Henning, T.; Petkov, B.; et al. Multi-seasonal ultrafine aerosol particle number concentration measurements at the Gruvebadet observatory, Ny-Ålesund, Svalbard Islands. *Rendiconti Lincei* **2016**, *27*, 59–71.
26. Mazzola, M.; Viola, A.P.; Lanconelli, C.; Vitale, V. Atmospheric observations at the Amundsen-Nobile Climate Change Tower in Ny-Ålesund, Svalbard. *Rendiconti Lincei* **2016**, *27*, 7–18.
27. Ferrero, L.; Sangiorgi, G.; Perrone, M.G.; Rizzi, C.; Cataldi, M.; Markuszewski, P.; Pakszys, P.; Makuch, P.; Petelski, T.; Becagli, S.; et al. Chemical Composition of Aerosol over the Arctic Ocean from Summer ARctic EXpedition (AREX) 2011–2012 Cruises: Ions, Amines, Elemental Carbon, Organic Matter, Polycyclic Aromatic Hydrocarbons, n-Alkanes, Metals, and Rare Earth Elements. *Atmosphere* **2019**, *10*, 54.

28. Ferrero, L.; Cappelletti, D.; Busetto, M.; Mazzola, M.; Lupi, A.; Lanconelli, C.; Becagli, S.; Traversi, R.; Caiazzo, L.; Giardi, F.; et al. Vertical profiles of aerosol and black carbon in the Arctic: A seasonal phenomenology along 2 years (2011–2012) of field campaigns. *Atmos. Chem. Phys.* **2016**, *16*, 12601–12629.
29. Ferrero, L.; Ritter, C.; Cappelletti, D.; Moroni, B.; Močnik, G.; Mazzola, M.; Lupi, A.; Becagli, S.; Traversi, R.; Cataldi, M.; et al. Aerosol optical properties in the Arctic: The role of aerosol chemistry and dust composition in a closure experiment between Lidar and tethered balloon vertical profiles. *Sci. Total Environ.* **2019**, *686*, 452–467.
30. Cappelletti, D.; Petroselli, C.; Mateos, D.; Herreras, M.; Ferrero, L.; Losi, N.; Gregorič, A.; Frangipani, C.; La Porta, G.; Lonardi, M.; et al. Vertical profiles of black carbon and nanoparticles pollutants measured by a tethered balloon in Longyearbyen (Svalbard islands). *Atmos. Environ.* **2022**, *290*, 119373.
31. Nicolaus, M.; Perovich, D.K.; Spreen, G.; Granskog, M.A.; von Albedyll, L.; Angelopoulos, M.; Anhaus, P.; Arndt, S.; Jakob Belter, H.; Bessonov, V.; et al. Overview of the MOSAiC expedition: Snow and sea ice. *Elementa* **2022**, *10*, 000046.
32. Shupe, M.D.; Rex, M.; Blomquist, B.; Persson, P.O.G.; Schmale, J.; Uttal, T.; Buck, C.; Boyer, M.; Hofer, J.; Hamilton, J.; et al. Overview of the MOSAiC expedition: Atmosphere. *Elementa* **2022**, *10*, 00060.
33. Regnery, J.; Aksenov, Y.; Allerholt, J.; Athanase, M.; Rabe, B.; Davies, A.; Damm, E.; Dethloff, K.; Divine, D.V.; Doglioni, F.; et al. Overview of the MOSAiC expedition: Physical oceanography. *Elem. Sci. Anthr.* **2022**, *10*, 00062.
34. Fong, A.A.; Hoppe, C.J.M.; Aberle, N.; Ashjian, C.J.; Assmy, P.; Bai, Y.; Bakker, D.C.E.; Balmonte, J.P.; Barry, K.R.; Bertilsson, S.; et al. Overview of the MOSAiC expedition: Ecosystem. *Elem. Sci. Anthr.* **2024**, *12*, 00135.
35. Mech, M.; Ehrlich, A.; Herber, A.; Lüpkes, C.; Wendisch, M.; Becker, S.; Boose, Y.; Chechin, D.; Crewell, S.; Dupuy, R.; et al. MOSAiC-ACA and AFLUX-Arctic airborne campaigns characterizing the exit area of MOSAiC. *Sci. Data* **2022**, *9*, 790.
36. Gulev, S.; Thorne, P.; Ahn, J.; Dentener, F.; Domingues, C.; Gerland, S.; Gong, D.; Kaufman, D.S.; Nnamchi, H.C.; Quaas, J.; et al. *The Changing State of the Climate*; Cambridge University Press: Cambridge, UK, 2021.
37. Swain, B.; Vountas, M.; Deroubaix, A.; Lelli, L.; Ziegler, Y.; Jafariserajehlou, S.; Gunthe, S.S.; Herber, A.; Ritter, C.; Bösch, H.; et al. Retrieval of aerosol optical depth over the Arctic cryosphere during spring and summer using satellite observations. *Atmos. Meas. Tech.* **2024**, *17*, 359–375.
38. Parkinson, C.L. Arctic sea ice coverage from 43 years of satellite passive-microwave observations. *Front. Remote Sens.* **2022**, *3*, 1021781.
39. Wang, X.; Liu, Y.; Key, J.R.; Dworak, R. A New Perspective on Four Decades of Changes in Arctic Sea Ice from Satellite Observations. *Remote Sens.* **2022**, *14*, 1846.
40. Crichton, K.A.; Anderson, K.; Fewster, R.E.; Charman, D.J.; Garneau, M.; Väliranta, M.; Mleczko, M.; Handley, J.N.; Hodson, S.; Parker, R.E.; et al. Satellite data indicates recent Arctic peatland expansion with warming. *Commun. Earth Environ.* **2025**, *6*, 461.
41. Bartsch, A.; Bergstedt, H.; Pointner, G.; Muri, X.; Rautiainen, K.; Leppänen, L.; Joly, K.; Sokolov, A.; Orekhov, P.; Ehrich, D.; et al. Towards long-term records of rain-on-snow events across the Arctic from satellite data. *Cryosphere* **2023**, *17*, 889–915.
42. Pithan, F.; Svensson, G.; Caballero, R.; Chechin, D.; Cronin, T.W.; Ekman, A.M.L.; Neggers, R.; Shupe, M.D.; Solomon, A.; Tjernström, M.; et al. Role of air-mass transformations in exchange between the Arctic and mid-latitudes. *Nat. Geosci.* **2018**, *11*, 805–812.
43. Cohen, J.; Screen, J.A.; Furtado, J.C.; Barlow, M.; Whittleston, D.; Coumou, D.; Francis, J.; Dethloff, K.; Entekhabi, D.; Overland, J.; et al. Recent Arctic amplification and extreme mid-latitude weather. *Nat. Geosci.* **2014**, *7*, 627–637.
44. Ren, L.; Yang, Y.; Wang, H.; Zhang, R.; Wang, P.; Liao, H. Source attribution of Arctic black carbon and sulfate aerosols and associated Arctic surface warming during 1980-2018. *Atmos. Chem. Phys.* **2020**, *20*, 9067–9085.
45. Sand, M.; Berntsen, T.K.; Kay, J.E.; Lamarque, J.F.; Seland, Ø.; Kirkevåg, A. The Arctic response to remote and local forcing of black carbon. *Atmos. Chem. Phys.* **2013**, *13*, 211–224.
46. Mewes, D.; Jacobi, C. Heat transport pathways into the Arctic and their connections to surface air temperatures. *Atmos. Chem. Phys.* **2019**, *19*, 3927–3937.
47. Graversen, R.G. Do changes in the midlatitude circulation have any impact on the Arctic surface air temperature trend? *J. Clim.* **2006**, *19*, 5422–5438.
48. Hahn, L.C.; Armour, K.C.; Battisti, D.S.; Donohoe, A.; Fajber, R. Seasonal Changes in Atmospheric Heat Transport to the Arctic Under Increased CO_2. *Geophys. Res. Lett.* **2023**, *50*, e2023GL105156.
49. Liu, Y.; Attema, J.; Moat, B.; Hazeleger, W. Synthesis and evaluation of historical meridional heat transport from midlatitudes towards the Arctic. *Earth Syst. Dyn.* **2020**, *11*, 77–96.
50. Bond, T.C.; Bergstrom, R.W. Light Absorption by Carbonaceous Particles: An Investigative Review. *Aerosol Sci. Technol.* **2006**, *40*, 27–67.

51. Laskin, A.; Laskin, J.; Nizkorodov, S.A. Chemistry of Atmospheric Brown Carbon. *Chem. Rev.* **2015**, *115*, 4335–4382.
52. Petzold, A.; Ogren, J.A.; Fiebig, M.; Laj, P.; Li, S.M.; Baltensperger, U.; Holzer-Popp, T.; Kinne, S.; Pappalardo, G.; Sugimoto, N.; et al. Recommendations for reporting black carbon measurements. *Atmos. Chem. Phys.* **2013**, *13*, 8365–8379.
53. Alexeev, V.A.; Jackson, C.H. Polar amplification: Is atmospheric heat transport important? *Clim. Dyn.* **2013**, *41*, 533–547.
54. Schmale, J.; Zieger, P.; Ekman, A.M.L. Aerosols in current and future Arctic climate. *Nat. Clim. Change* **2021**, *11*, 95–105.
55. Law, K.S.; Stohl, A. Arctic air pollution: Origins and impacts. *Science* **2007**, *315*, 1537–1540.
56. Beck, L.J.; Sarnela, N.; Junninen, H.; Hoppe, C.J.M.; Garmash, O.; Bianchi, F.; Riva, M.; Rose, C.; Peräkylä, O.; Wimmer, D.; et al. Differing Mechanisms of New Particle Formation at Two Arctic Sites. *Geophys. Res. Lett.* **2021**, *48*, e2020GL091334.
57. Groot Zwaaftink, C.D.; Grythe, H.; Skov, H.; Stohl, A. Substantial contribution of northern high-latitude sources to mineral dust in the Arctic. *J. Geophys. Res.* **2016**, *121*, 13678–13697.
58. Yasunari, T.J.; Koster, R.D.; Lau, W.K.M.; Kim, K. Journal of geophysical research. *Nature* **1955**, *175*, 238.
59. Flanner, M.G. Arctic climate sensitivity to local black carbon. *J. Geophys. Res. Atmos.* **2013**, *118*, 1840–1851.
60. Ban-Weiss, G.A.; Cao, L.; Bala, G.; Caldeira, K. Dependence of climate forcing and response on the altitude of black carbon aerosols. *Clim. Dyn.* **2011**, *38*, 897–911.
61. Ramana, M.V.; Ramanathan, V.; Kim, D.; Roberts, G.C.; Corrigan, C.E. Albedo , atmospheric solar absorption and heating rate measurements with stacked UAVs. *Q. J. R. Meteorol. Soc.* **2007**, *133*, 1913–1931.
62. Schwarz, J.P.; Samset, B.H.; Perring, A.E.; Spackman, J.R.; Gao, R.S.; Stier, P.; Schulz, M.; Moore, F.L.; Ray, E.A.; Fahey, D.W. Global-scale seasonally resolved black carbon vertical profiles over the Pacific. *Geophys. Res. Lett.* **2013**, *40*, 5542–5547.
63. Samset, B.H.; Myhre, G.; Herber, A.; Kondo, Y.; Li, S.-M.; Moteki, N.; Koike, M.; Oshima, N.; Schwarz, J.P.; Balkanski, Y.; et al. Modelled black carbon radiative forcing and atmospheric lifetime in AeroCom Phase II constrained by aircraft observations. *Atmos. Chem. Phys.* **2014**, *14*, 12465–12477.
64. Ferrero, L.; Castelli, M.; Ferrini, B.S.; Moscatelli, M.; Perrone, M.G.; Sangiorgi, G.; D'Angelo, L.; Rovelli, G.; Moroni, B.; Scardazza, F.; et al. Impact of black carbon aerosol over Italian basin valleys: High-resolution measurements along vertical profiles, radiative forcing and heating rate. *Atmos. Chem. Phys.* **2014**, *14*, 9641–9664.
65. Brock, C.A.; Cozic, J.; Bahreini, R.; Froyd, K.D.; Middlebrook, A.M.; McComiskey, A.; Brioude, J.; Cooper, O.R.; Stohl, A.; Aikin, K.C.; et al. Characteristics, sources, and transport of aerosols measured in spring 2008 during the aerosol, radiation, and cloud processes affecting Arctic Climate (ARCPAC) Project. *Atmos. Chem. Phys.* **2011**, *11*, 2423–2453.
66. Ferrero, L.; Cappelletti, D.; Moroni, B.; Sangiorgi, G.; Perrone, M.G.; Crocchianti, S.; Bolzacchini, E. Wintertime aerosol dynamics and chemical composition across the mixing layer over basin valleys. *Atmos. Environ.* **2012**, *56*, 143–153.
67. Su, T.; Li, Z.; Li, C.; Li, J.; Han, W.; Shen, C.; Tan, W.; Wei, J.; Guo, J. The significant impact of aerosol vertical structure on lower atmosphere stability and its critical role in aerosol–planetary boundary layer (PBL) interactions. *Atmos. Chem. Phys.* **2020**, *20*, 3713–3724.
68. Navarro, J.C.A.; Varma, V.; Riipinen, I.; Seland, Ø.; Kirkevåg, A.; Struthers, H.; Iversen, T.; Hansson, H.C.; Ekman, A.M.L. Amplification of Arctic warming by past air pollution reductions in Europe. *Nat. Geosci.* **2016**, *9*, 277–281.
69. Wu, Y.T.; Liang, Y.C.; Previdi, M.; Polvani, L.M.; England, M.R.; Sigmond, M.; Lo, M.H. Stronger Arctic amplification from anthropogenic aerosols than from greenhouse gases. *npj Clim. Atmos. Sci.* **2024**, *7*, 142.
70. Samset, B.H.; Myhre, G.; Schulz, M.; Balkanski, Y.; Bauer, S.; Berntsen, T.K.; Bian, H.; Bellouin, N.; Diehl, T.; Easter, R.C.; et al. Black carbon vertical profiles strongly affect its radiative forcing uncertainty. *Atmos. Chem. Phys.* **2013**, *13*, 2423–2434.
71. Losi, N.; Markuszewski, P.; Rigler, M.; Gregorič, A.; Močnik, G.; Drozdowska, V.; Makuch, P.; Zielinski, T.; Pakszys, P.; Kitowska, M.; et al. Anthropic Settlements ' Impact on the Light-Absorbing Aerosol Concentrations and Heating Rate in the Arctic. *Atmosphere* **2023**, *14*, 1768.
72. Ferrero, L.; Scibetta, L.; Markuszewski, P.; Mazurkiewicz, M.; Drozdowska, V.; Makuch, P.; Jutrzenka-Trzebiatowska, P.; Zaleska-Medynska, A.; Andò, S.; Saliu, F.; et al. Airborne and marine microplastics from an oceanographic survey at the Baltic Sea: An emerging role of air-sea interaction? *Sci. Total Environ.* **2022**, *824*, 153709.
73. Savadkoohi, M.; Pandolfi, M.; Favez, O.; Putaud, J.P.; Eleftheriadis, K.; Fiebig, M.; Hopke, P.K.; Laj, P.; Wiedensohler, A.; Alados-Arboledas, L.; et al. Recommendations for reporting equivalent black carbon (eBC) mass concentrations based on long-term pan-European in-situ observations. *Environ. Int.* **2024**, *185*, 108553.
74. Wood, J.; Smyth, T.J.; Estellés, V. Autonomous marine hyperspectral radiometers for determining solar irradiances and aerosol optical properties. *Atmos. Meas. Tech.* **2017**, *10*, 1723–1737.
75. Long, C.N.; Bucholtz, A.; Jonsson, H.; Schmid, B.; Vogelmann, A.; Wood, J. A Method of Correcting for Tilt from Horizontal in Downwelling Shortwave Irradiance Measurements on Moving Platforms. *Open Atmos. Sci. J.* **2010**, *4*, 78–87.

76. Ehnberg, J.S.G.; Bollen, M.H.J. Simulation of global solar radiation based on cloud observations. *Sol. Energy* **2005**, *78*, 157–162.
77. Ferrero, L.; Gregorič, A.; Močnik, G.; Rigler, M.; Cogliati, S.; Barnaba, F.; Liberto, L.D.; Gobbi, G.P.; Losi, N.; Bolzacchini, E. The impact of cloudiness and cloud type on the atmospheric heating rate of black and brown carbon in the Po Valley. *Atmos. Chem. Phys.* **2021**, *21*, 4869–4897.
78. Cogliati, S.; Rossini, M.; Julitta, T.; Meroni, M.; Schickling, A.; Burkart, A.; Pinto, F.; Rascher, U.; Colombo, R. Continuous and long-term measurements of reflectance and sun-induced chlorophyll fluorescence by using novel automated field spectroscopy systems. *Remote Sens. Environ.* **2015**, *164*, 270–281.
79. Ferrero, L.; Močnik, G.; Cogliati, S.; Gregorič, A.; Colombo, R.; Bolzacchini, E. Heating Rate of Light Absorbing Aerosols: Time-Resolved Measurements, the Role of Clouds, and Source Identification. *Environ. Sci. Technol.* **2018**, *52*, 3546–3555.
80. Ferrero, L.; Bernardoni, V.; Santagostini, L.; Cogliati, S.; Soldan, F.; Valentini, S.; Massabò, D.; Močnik, G.; Gregorič, A.; Rigler, M.; et al. Consistent determination of the heating rate of light-absorbing aerosol using wavelength- and time-dependent Aethalometer multiple-scattering correction. *Sci. Total Environ.* **2021**, *791*, 148277.
81. David, J.; D'ANgelo, L.; Gregorič, A.; Rigler, M.; Moschos, V.; Ferrero, L.; Vogel, A.L. Nocturnal agricultural fires contribute to secondary brown carbon in the rural Po Valley. *Environ. Sci. Atmos.* **2026**, *6*, 1453–1467.
82. Drinovec, L.; Močnik, G.; Zotter, P.; Prévôt, A.S.H.; Ruckstuhl, C.; Coz, E.; Rupakheti, M.; Sciare, J.; Müller, T.; Wiedensohler, A.; et al. The "dual-spot" Aethalometer: An improved measurement of aerosol black carbon with real-time loading compensation. *Atmos. Meas. Tech.* **2015**, *8*, 1965–1979.
83. Coen, M.C.; Andrews, E.; Lastuey, A.; Arsov, T.P.; Backman, J.; Brem, B.T.; Bukowiecki, N.; Couret, C.; Eleftheriadis, K.; Flentje, H.; et al. Multidecadal trend analysis of in situ aerosol radiative properties around the world. *Atmos. Chem. Phys.* **2020**, *20*, 8867–8908.
84. Bond, T.C.; Doherty, S.J.; Fahey, D.W.; Forster, P.M.; Berntsen, T.; Deangelo, B.J.; Flanner, M.G.; Ghan, S.; Kärcher, B.; Koch, D.; et al. Bounding the role of black carbon in the climate system: A scientific assessment. *J. Geophys. Res. Atmos.* **2013**, *118*, 5380–5552.
85. Moosmüller, H.; Chakrabarty, R.K.; Arnott, W.P. Aerosol light absorption and its measurement: A review. *J. Quant. Spectrosc. Radiat. Transf.* **2009**, *110*, 844–878.
86. Baumgardner, D.; Popovicheva, O.; Allan, J.; Bernardoni, V.; Cao, J.; Cavalli, F.; Cozic, J.; Diapouli, E.; Eleftheriadis, K.; Genberg, P.J.; et al. Soot reference materials for instrument calibration and intercomparisons: A workshop summary with recommendations. *Atmos. Meas. Tech.* **2012**, *5*, 1869–1887.
87. Backman, J.; Schmeisser, L.; Virkkula, A.; Ogren, J.A.; Asmi, E.; Starkweather, S.; Sharma, S.; Eleftheriadis, K.; Uttal, T.; Jefferson, A.; et al. On Aethalometer measurement uncertainties and an instrument correction factor for the Arctic. *Atmos. Meas. Tech.* **2017**, *10*, 5039–5062.
88. Savadkoohi, M.; Pandolfi, M.; Reche, C.; Niemi, J.V.; Mooibroek, D.; Titos, G.; Green, D.C.; Tremper, A.H.; Hueglin, C.; Liakakou, E.; et al. The variability of mass concentrations and source apportionment analysis of equivalent black carbon across urban Europe. *Environ. Int.* **2023**, *178*, 108081.
89. Yus-Díez, J.; Bernardoni, V.; Močnik, G.; Alastuey, A.; Ciniglia, D.; Ivančič, M.; Querol, X.; Perez, N.; Reche, C.; Rigler, M.; et al. Determination of the multiple-scattering correction factor and its cross-sensitivity to scattering and wavelength dependence for different AE33 Aethalometer filter tapes: A multi-instrumental approach. *Atmos. Meas. Tech.* **2021**, *14*, 6335–6355.
90. Ferrero, L.; Losi, N.; Rigler, M.; Gregorič, A.; Colombi, C.; D'Angelo, L.; Cuccia, E.; Cefalì, A.M.; Gini, I.; Doldi, A.; et al. Determining the Aethalometer multiple scattering enhancement factor C from the filter loading parameter. *Sci. Total Environ.* **2024**, *917*, 170221.
91. Weingartner, E.; Saathoff, H.; Schnaiter, M.; Streit, N.; Bitnar, B.; Baltensperger, U. Absorption of light by soot particles: Determination of the absorption coefficient by means of aethalometers. *J. Aerosol Sci.* **2003**, *34*, 1445–1463.
92. Yus-Díez, J.; Drinovec, L.; Alados-Arboledas, L.; Titos, G.; Bazo, E.; Casans, A.; Patrón, D.; Querol, X.; Gonzalez-Romero, A.; Perez García-Pando, C.; et al. Characterization of filter photometer artifacts in soot and dust measurements-Laboratory and ambient experiments using a traceably calibrated aerosol absorption reference. *Atmos. Meas. Tech.* **2025**, *18*, 3073–3093.
93. Ivančič, M.; Gregorič, A.; Lavrič, G.; Alföldy, B.; Ježek, I.; Hasheminassab, S.; Pakbin, P.; Ahangar, F.; Sowlat, M.; Boddeker, S.; et al. Two-year-long high-time-resolution apportionment of primary and secondary carbonaceous aerosols in the Los Angeles Basin using an advanced total carbon–black carbon (TC-BC(λ)) method. *Sci. Total Environ.* **2022**, *848*, 157606.
94. Ferrero, L.; Riccio, A.; Ferrini, B.S.; D'Angelo, L.; Rovelli, G.; Casati, M.; Angelini, F.; Barnaba, F.; Gobbi, G.P.; Cataldi, M.; et al. Satellite AOD conversion into ground PM10, PM2.5 and PM1 over the Po valley (Milan, Italy) exploiting information on aerosol vertical profiles, chemistry, hygroscopicity and meteorology. *Atmos. Pollut. Res.* **2019**, *10*, 1895–1912.

95. Danabasoglu, G.; Lamarque, J.F.; Bacmeister, J.; Bailey, D.A.; DuVivier, A.K.; Edwards, J.; Emmons, L.K.; Fasullo, J.; Garcia, R.; Gettelman, A.; et al. The Community Earth System Model Version 2 (CESM2). *J. Adv. Model. Earth Syst.* **2020**, *12*, e2019MS001916.
96. Hurrell, J.W.; Hack, J.J.; Shea, D.; Caron, J.M.; Rosinski, J. A new sea surface temperature and sea ice boundary dataset for the community atmosphere model. *J. Clim.* **2008**, *21*, 5145–5153.
97. Bogenschutz, P.A.; Gettelman, A.; Hannay, C.; Larson, V.E.; Neale, R.B.; Craig, C.; Chen, C.C. The path to CAM6: Coupled simulations with CAM5.4 and CAM5.5. *Geosci. Model Dev.* **2018**, *11*, 235–255.
98. Lawrence, D.M.; Fisher, R.A.; Koven, C.D.; Oleson, K.W.; Swenson, S.C.; Bonan, G.; Collier, N.; Ghimire, B.; van Kampenhout, L.; Kennedy, D.; et al. The Community Land Model Version 5: Description of New Features, Benchmarking, and Impact of Forcing Uncertainty. *J. Adv. Model. Earth Syst.* **2019**, *11*, 4245–4287.
99. Zhang, J.; Huang, P. Uncertainty of the Future Changes in Interannual Precipitation Variability under Global Warming Based on Single-Model Initial-Condition Large Ensembles and CMIP6. *Adv. Atmos. Sci.* **2025**, *42*, 2279–2289.
100. Tian, P.; Liu, D.; Zhao, D.; Yu, C.; Liu, Q.; Huang, M.; Deng, Z.; Ran, L.; Wu, Y.; Ding, S.; et al. In-situ vertical characteristics of optical properties and heating rates of aerosol over Beijing. *Atmos. Chem. Phys. Discuss.* **2019**, *20*, 2603–2622.
101. Liu, J.; Fan, S.; Horowitz, L.W.; Levy, H. Evaluation of factors controlling long-range transport of black carbon to the Arctic. *J. Geophys. Res. Atmos.* **2011**, *116*, D04307.
102. Liu, H.; Pan, X.; Lei, S.; Zhang, Y.; Du, A.; Yao, W.; Tang, G.; Wang, T.; Xin, J.; Li, J.; et al. Vertical distribution of black carbon and its mixing state in the urban boundary layer in summer. *Atmos. Chem. Phys.* **2023**, *23*, 7225–7239.
103. Jurányi, Z.; Zanatta, M.; Lund, M.T.; Samset, B.H.; Skeie, R.B.; Sharma, S.; Wendisch, M.; Herber, A. Atmospheric concentrations of black carbon are substantially higher in spring than summer in the Arctic. *Commun. Earth Environ.* **2023**, *4*, 91.
104. Spackman, J.R.; Gao, R.S.; Neff, W.D.; Schwarz, J.P.; Watts, L.A.; Fahey, D.W.; Holloway, J.S.; Ryerson, T.B.; Peischl, J.; Brock, C. a. Aircraft observations of enhancement and depletion of black carbon mass in the springtime Arctic. *Atmos. Chem. Phys.* **2010**, *10*, 9667–9680.
105. Schwarz, J.P.; Spackman, J.R.; Gao, R.S.; Watts, L.A.; Stier, P.; Schulz, M.; Davis, S.M.; Wofsy, S.C.; Fahey, D.W. Global-scale black carbon profiles observed in the remote atmosphere and compared to models. *Geophys. Res. Lett.* **2010**, *37*, L18812.
106. Schwarz, J.P.; Weinzierl, B.; Samset, B.H.; Dollner, M.; Heimerl, K.; Markovic, M.Z.; Perring, A.E.; Ziemba, L. Aircraft measurements of black carbon vertical profiles show upper tropospheric variability and stability. *Geophys. Res. Lett.* **2017**, *44*, 1132–1140.
107. Zanatta, M.; Mertes, S.; Jourdan, O.; Dupuy, R.; Järvinen, E.; Schnaiter, M.; Eppers, O.; Schneider, J.; Jurányi, Z.; Herber, A. Airborne investigation of black carbon interaction with low-level, persistent, mixed-phase clouds in the Arctic summer. *Atmos. Chem. Phys.* **2023**, *23*, 7955–7973.
108. Preece, J.R.; Mote, T.L.; Cohen, J.; Wachowicz, L.J.; Knox, J.A.; Tedesco, M.; Kooperman, G.J. Summer atmospheric circulation over Greenland in response to Arctic amplification and diminished spring snow cover. *Nat. Commun.* **2023**, *14*, 3759.
109. Stjern, C.W.; Samset, B.H.; Myhre, G.; Forster, P.M.; Hodnebrog, Ø.; Andrews, T.; Boucher, O.; Faluvegi, G.; Iversen, T.; Kasoar, M.; et al. Rapid Adjustments Cause Weak Surface Temperature Response to Increased Black Carbon Concentrations. *J. Geophys. Res. Atmos.* **2017**, *122*, 11462–11481.
110. Smith, C.J.; Kramer, R.J.; Myhre, G.; Forster, P.M.; Soden, B.J.; Andrews, T.; Boucher, O.; Faluvegi, G.; Fläschner, D.; Hodnebrog, Ø.; et al. Understanding Rapid Adjustments to Diverse Forcing Agents. *Geophys. Res. Lett.* **2018**, *45*, 12023–12031.
111. Fajber, R.; Donohoe, A.; Ragen, S.; Armour, K.C.; Kushner, P.J. Atmospheric heat transport is governed by meridional gradients in surface evaporation in modern-day earth-like climates. *Proc. Natl. Acad. Sci. USA* **2023**, *120*, e2217202120.
112. Needham, M.R.; Randall, D.A. Anomalous Northward Energy Transport due to Anthropogenic Aerosols during the Twentieth Century. *J. Clim.* **2023**, *36*, 6713–6728.
113. Xing, J.; Bian, L.; Hu, Q.; Yu, J.; Sun, C.; Xie, Z. Atmospheric black carbon along a cruise path through the arctic ocean during the fifth Chinese arctic research expedition. *Atmosphere* **2014**, *5*, 292–306.
114. Heintzenberg, J.; Leck, C. Seasonal variation of the atmospheric aerosol near the top of the marine boundary layer over Spitsbergen related to the Arctic sulphur cycle. *Tellus B Chem. Phys. Meteorol.* **1994**, *46*, 52–67.
115. Matsui, H.; Liu, M. Importance of supersaturation in arctic black carbon simulations. *J. Clim.* **2021**, *34*, 7843–7856.
116. Cape, J.N.; Coyle, M.; Dumitrean, P. The atmospheric lifetime of black carbon. *Atmos. Environ.* **2012**, *59*, 256–263.
117. Fajber, R.; Kushner, P.J.; Laliberté, F. Influence of midlatitude surface thermal anomalies on the polar midtroposphere in an idealized moist model. *J. Atmos. Sci.* **2018**, *75*, 1089–1104.
118. Willis, M.D.; Bozem, H.; Kunkel, D.; Lee, A.K.Y.; Schulz, H.; Burkart, J.; Aliabadi, A.A.; Herber, A.B.; Richard Leaitch, W.; Abbatt, J.P.D. Aircraft-based measurements of High Arctic springtime aerosol show evidence for vertically varying sources, transport and composition. *Atmos. Chem. Phys.* **2019**, *19*, 57–76.

119. Lu, J.; Cai, M. Seasonality of polar surface warming amplification in climate simulations. *Geophys. Res. Lett.* **2009**, *36*, L16704.
120. Yang, X.Y.; Fyfe, J.C.; Flato, G.M. The role of poleward energy transport in arctic temperature evolution. *Geophys. Res. Lett.* **2010**, *37*, L14803.
121. Audette, A.; Fajber, R.A.; Kushner, P.J.; Wu, Y.; Peings, Y.; Magnusdottir, G.; Eade, R.; Sigmond, M.; Sun, L. Opposite Responses of the Dry and Moist Eddy Heat Transport Into the Arctic in the PAMIP Experiments. *Geophys. Res. Lett.* **2021**, *48*, e2020GL089990.
122. Yim, B.Y.; Yeh, S.W.; Kug, J.S. Inter-model diversity of Arctic amplification caused by global warming and its relationship with the Inter-tropical Convergence Zone in CMIP5 climate models. *Clim. Dyn.* **2017**, *48*, 3799–3811.
123. Francis, J.A.; Vavrus, S.J.; Cohen, J. Amplified Arctic warming and mid-latitude weather: New perspectives on emerging connections. *Wiley Interdiscip. Rev. Clim. Change* **2017**, *8*, e474.
124. Baggett, C.; Lee, S. Arctic warming induced by tropically forced tapping of available potential energy and the role of the planetary-scale waves. *J. Atmos. Sci.* **2015**, *72*, 1562–1568.
125. Baggett, C.; Lee, S.; Feldstein, S. An investigation of the presence of atmospheric rivers over the North Pacific during planetary-scale wave life cycles and their role in Arctic warming. *J. Atmos. Sci.* **2016**, *73*, 4329–4347.
126. Baggett, C.; Lee, S. An identification of the mechanisms that lead to arctic warming during planetary-scale and synoptic-scale wave life cycles. *J. Atmos. Sci.* **2017**, *74*, 1859–1877.
127. Graversen, R.G.; Langen, P.L. On the role of the atmospheric energy transport in 2×3CO2-induced polar amplification in CESM1. *J. Clim.* **2019**, *32*, 3941–3956.
128. Vestreng, V.; Myhre, G.; Fagerli, H.; Reis, S.; Tarrasón, L. Twenty-five years of continuous sulphur dioxide emission reduction in Europe. *Atmos. Chem. Phys.* **2007**, *7*, 3663–3681.
129. Monks, P.S.; Granier, C.; Fuzzi, S.; Stohl, A.; Williams, M.L.; Akimoto, H.; Amann, M.; Baklanov, A.; Baltensperger, U.; Bey, I.; et al. Atmospheric composition change–global and regional air quality. *Atmos. Environ.* **2009**, *43*, 5268–5350.
130. Shindell, D.; Kuylenstierna, J.C.I.; Vignati, E.; van Dingenen, R.; Klimont, Z.; Anenberg, S.C.; Muller, N.; Janssens-Maenhout, G.; Raes, F.; Schwartz, J.; et al. Simultaneously Mitigating Near-Term Climate Change and Improving Human Health adn Food Security. *Science* **2012**, *335*, 183–189.
131. Jacobson, M.Z. Control of fossil-fuel particulate black carbon and organic matter, possibly the most effective method of slowing global warming. *J. Geophys. Res.* **2002**, *107*, 4410.

Disclaimer/Publisher's Note: The statements, opinions and data contained in all publications are solely those of the individual author(s) and contributor(s) and not of MDPI and/or the editor(s). MDPI and/or the editor(s) disclaim responsibility for any injury to people or property resulting from any ideas, methods, instructions or products referred to in the content.